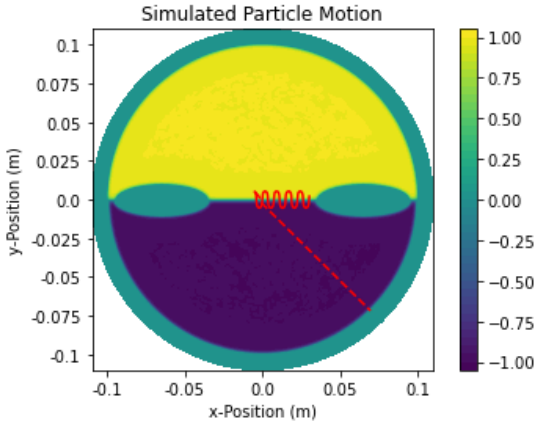

Detecting Dark Domain Walls in a Topologically-Tailored Vacuum Chamber

by Kate E. A. Clements, MSci, MMath

Thesis submitted to the University of Nottingham
for the degree of Doctor of Philosophy, January 22, 2025

Supervised by T. M. Fromhold & C. Burrage

University of Nottingham
UK | CHINA | MALAYSIA

Abstract

We propose a laboratory experiment to detect the fifth force mediated by a new light scalar field. The symmetron is a light scalar field which couples quadratically to matter, with a symmetry-breaking potential that takes the form of a symmetric double well. As the characteristic phase transition of the symmetron field occurs, topological defects or 'domain walls' can form. It is hoped that by designing and manufacturing a topologically-tailored vacuum chamber, we can ensure that these domain walls are long-lived by pinning them to the interior of the chamber. A good vacuum will result in a very low density environment in which the symmetron can couple to matter with gravitational strength, or more strongly, and the effects of the scalar field on a matter particle are potentially observable via a particle experiment involving ultracold atoms. As a cloud of cold atoms approaches the domain wall, it will experience the fifth force mediated by the scalar field and can be deflected or reflected off the domain wall. We also consider the effects of domain walls on light that passes through them. The deflection or reflection of matter due to the presence of a domain wall is a signature of the fifth force and could constrain some previously unconstrained parts of the dark sector.

Acknowledgements

Firstly to all my colleagues at Nottingham, and especially my friends in office C19. Thank you for all the laughs, and for making studying for a PhD during a global pandemic not just bearable but fun. To my supervisor Clare, who is an inspiring person to work with. Thank you for your endless patience and generosity with your time, and for making me feel like no question was too silly. To Mark, who has been not just my supervisor but my mentor for the past 11 years. Thanks for always believing in my abilities when I didn't; I couldn't have done this without you.

On a more personal note: to my parents, who have always been and continue to be my biggest supporters. Thank you for giving me the freedom to choose my own path in life, and for insisting on reading everything that I write no matter how interesting or good it is (or isn't). Lastly to my partner Chris, who has been by my side through two Master's degrees and a PhD — I'm very sorry for all the second-hand stress. Thanks for being the best partner in crime I could have ever asked for (and for doing all the household chores while I wrote this thesis).

Contents

Chapter 1

Introduction

Many theories in high energy physics predict the existence of new light scalar fields that couple to gravity (see for example [1, 2]). These light scalar fields are of particular interest in theories pertaining to the dark sector, since they have the potential to play the role of dark matter or dark energy. The general method for modelling this class of modified gravity theory is to alter the Klein–Gordon equation,

$$(-\partial_t^2 + \nabla^2 - m^2)\phi(t, \mathbf{x}) = 0, \tag{1.1}$$

to include a new light scalar field that couples to matter. Although these new light scalar fields have proven to be popular in theories of modified gravity, they are yet to be observed in any experiment designed to detect the 'fifth force' that arises due to the coupling of the scalar field to matter [3, 4].

There have been several proposals for methods by which new light scalar fields can evade detection in experiments. The first of these proposals was the chameleon mechanism [1, 5], in which the scalar field is coupled to matter such that its effective mass is dependent on the local matter density. For any experiment performed where the local matter density is high, the scalar field will acquire a mass, which causes its effects to become short range. The field is thus 'screened' and its effects are unobservable. In this work we investigate a different method of screening called the symmetron mechanism. The symmetron mechanism is similar to the chameleon, with a few key differences: firstly, in the symmetron mechanism it is the expectation value of the field that depends on the local matter density [6]. The expectation value is large in regions of low local matter density, and small in regions of high local matter density. As in the chameleon mechanism, the scalar mediating the symmetron field must couple to matter and we choose to introduce nonlinearities in the Klein–Gordon equation to facilitate the screening behaviour that allows the fifth force to hide from detection in experiments. However, for the symmetron the coupling to matter is proportional to the expectation value of the field, such that the scalar will couple with gravitational strength in regions of low mass density but is decoupled and screened in regions of high mass density.

We propose an experiment to detect the fifth force mediated by a new light scalar field that can play the role of dark matter [7–11] or dark energy [6, 12]. There exists a previously unexplored region of parameter space in which a vacuum chamber can nullify any outside effects and thus make the effects of the fifth force detectable. A good vacuum will result in a very low density environment in which the symmetron can couple with gravitational strength, and the effects of the scalar field on a matter particle are potentially observable. Symmetron theories include a characteristic phase transition; cosmologically speaking, this transition occurs as the universe expands and cools [12]. High densities correspond to early times in the expansion of the universe, and low densities correspond to late times. As the phase transition occurs, topological defects or 'domain walls' can form. In the context of a tabletop experiment, we expect domain walls to form as the density of a vacuum chamber is lowered. It is hoped that by designing and manufacturing a topologically-tailored vacuum chamber, we can ensure that these domain walls are long-lived by pinning them to the interior of the chamber. We can then perform a particle experiment in which a matter particle is incident on a domain wall. As the matter particle approaches the domain wall, it will experience the fifth force mediated by the scalar field and will be deflected or possibly even reflected off the domain wall. This deflection or reflection is a signature of the fifth force and could constrain some previously unconstrained parts of the dark sector.

1.1 Domain walls

A domain wall is a class of topological defect, which forms when a discrete symmetry is broken [13]. The idea of topological defect formation dates back to 1961, when Skyrme described the first three-dimensional topological defect solution arising in a nonlinear field theory, and how this solution could be relevant in particle physics [14]. Since then, the significance of topological defect solutions has somewhat evolved; Skyrme and others [15, 16] initially proposed that the particle-like nature of defect states could be used to explain the observed spectrum of particle excitations. However, topological defects are

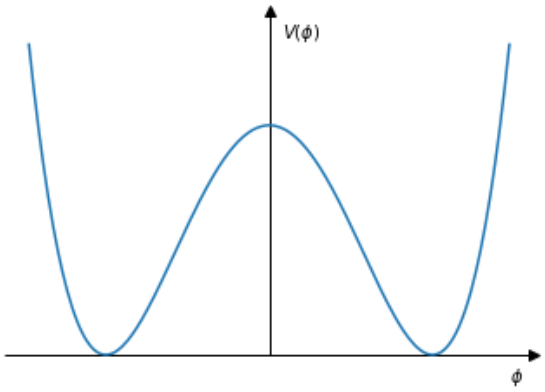

Figure 1.1: The potential given in Equation 1.2 defining a simple Goldstone model with a single real scalar field.

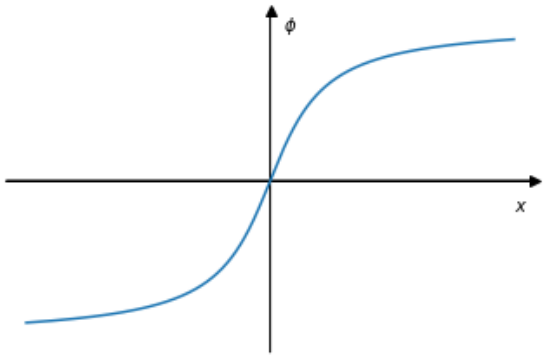

Figure 1.2: The analytical solution in Equation 1.3 for the simple Goldstone model.

now more commonly viewed as a consequence of spontaneous symmetry breaking, which results in a vacuum manifold with non-trivial topology.

The first known mention of domain walls in the context of cosmology was courtesy of Nambu in 1966 [17], although his idea that the Universe 'may have a kind of domain structure' was not thoroughly explored until the mid-1970s. Interest in cosmological domain walls increased in 1974, when Zel'dovich, Kobzarev and Okun published an article describing the properties of domain walls and their causally inevitable nature [18]. Weinberg was at this time studying the concept of cosmological domains [19], which led Everett to investigate the possibility of interactions between domain walls and matter [20]. The first quantitative study of domain wall formation was carried out in 1976 by Kibble [21], who showed that the existence of domain walls is dependent on the topology of the vacuum manifold. Domain walls form at the boundaries between regions of space in which the scalar field ϕ has two separate values, and ϕ is interpolated between these two values across the wall. We describe the formation of domain walls via the Kibble–Zurek mechanism in more detail in Section 3.1. First, to illustrate the concept of a domain wall in a simple way, we can consider a Goldstone model with a single real scalar field. This model is characterized by the following potential:

$$V(\phi) = \frac{\lambda}{4}\left(\phi^2 - \eta^2\right)^2, \tag{1.2}$$

as shown in Figure 1.1. One possible analytical solution to the field equation associated with this model is

$$\phi(x) = \eta \tanh\left((\lambda/2)^{1/2}\,\eta x\right), \tag{1.3}$$

as shown in Figure 1.2. This is sometimes referred to as a 'kink' solution centred at $x = 0$, with the boundary conditions:

$$\phi = -\eta \text{ at } x = -\infty \tag{1.4a}$$

$$\text{and } \phi = \eta \text{ at } x = +\infty. \tag{1.4b}$$

On the left-hand side of the kink, the field lies in one minimum of the potential, and on the right-hand side it lies in the opposite minimum. The discrete symmetry of the scalar field ϕ is spontaneously broken when the field must roll into one of the two degenerate minima. The topological defect is classically stable, as its removal would necessitate the lifting of the field solution on one side over the potential hill of the double well [13]. Since domain walls can couple to matter, it is feasible that we can exploit this coupling to find observational evidence of the effects of the fifth force associated with the domain wall formation. Using the equations of motion of a domain wall and a matter particle coupled to the wall, we can calculate the reflection and transmission coefficients corresponding to the interaction of the particle with the wall. We describe this calculation in detail in Section 2.3. The observation of the deflection or reflection of a matter particle off a domain wall would constitute experimental evidence of the fifth force.

1.2 Previous numerical studies of domain wall formation

Early simulations of domain wall evolution were carried out in 1989 by Press, Ryden and Spergel [22], and in 1990 by Kawano [23]. In both approaches the authors simplify their models, but in different ways: whereas Kawano chooses to approximate the domain walls as infinitely thin sheets, Press, Ryden and Spergel study the evolution of domain walls throughout space. Although arguably a much more realistic representation of physical domain walls, this method is not without limitation: for computational reasons, the authors modified the scalar field equation such that the thickness of the domain wall is time-dependent; the thickness increases as the scale factor of the universe increases. This simplification can cause issues such as erasing the small-scale structure of the domain walls, or eliminating a wall completely when its thickness becomes comparable to its size.

Many numerical models of domain wall formation rely on the quasistatic approximation; time derivatives are neglected in the solution of the scalar field's equation of motion [24–27]. However, more recent simulations of domain wall dynamics in the symmetron model have succeeded in solving the full equation of motion for the scalar field without the need for this approximation. Llinares and Pogosian [28] present a 2D simulation of a domain wall in a vacuum passing through a set of filaments, showing that a domain wall can be trapped as a consequence of the direct coupling of the symmetron field to matter. Similarly, it has been shown by Pearson [29] that domain walls are attracted to matter structures, and these structures can be used to stabilize the domain walls and 'pin' them in place. On cosmological scales, numerical simulations have been used to show that domain walls could be used to explain the observed planes of satellite galaxies around the Milky Way and Andromeda [30], or cause cosmic voids to be emptier [31]. It has also been suggested that a network of cosmological domain walls could source the nanohertz gravitational-wave background [32–35]. Very recently, the first cosmological simulations of the symmetron scalar field including domain wall formation have been performed [36]. Christiansen and colleagues use a relativistic N-body code to model domain wall

formation, and its effects on cosmological observables and structure formation. They also use this code to show that the dynamics of the dark sector can give rise to domain walls which source stochastic gravitational waves in the late Universe [37].

1.3 Spherically symmetric solution for the symmetron field

For astrophysical tests of gravity, the source may often be approximated as spherical; for this reason, we first look at the symmetron field profile around a spherical source. We make an initial choice for the symmetry-breaking potential V associated with the symmetron field ϕ:

$$V = -\frac{1}{2}\mu^2\phi^2 + \frac{1}{4}\lambda^2\phi^4 \tag{1.5}$$

where μ is a mass scale and λ is a dimensionless coupling. For non-relativistic matter for which the density ρ is roughly homogeneous, the symmetron field evolves according to an effective potential [6]

$$V_{\text{eff}}(\phi) = V(\phi) + \rho A(\phi) \tag{1.6}$$

where

$$A(\phi) = 1 + \frac{1}{2M^2}\phi^2 \tag{1.7}$$

and the matter density $\rho = A^3\tilde{\rho}$ is conserved in the Einstein frame. M is a mass scale, and $A(\phi)$ is the conformal factor relating the Einstein and Jordan frame metrics:

$$\tilde{g_{ab}} = A^2(\phi)\, g_{ab}. \tag{1.8}$$

In terms of these quantities, the symmetron field equation can be written as

$$\frac{\mathrm{d}^2}{\mathrm{d}r^2}\phi + \frac{2}{r}\frac{\mathrm{d}}{\mathrm{d}r}\phi = V_{,\phi} + A_{,\phi}\rho, \tag{1.9}$$

in our time-independent and spherically symmetric approximation. The boundary conditions for Equation 1.9 are [12]

$$\frac{\mathrm{d}}{\mathrm{d}r}\phi(0) = 0 \tag{1.10a}$$

$$\text{and } \phi(r \to \infty) = \phi_0, \tag{1.10b}$$

where $\phi_0 \equiv \phi(0)$ is the value of the field at $x = 0$. Equation 1.9 is analogous to a particle rolling in a potential $-V_{\text{eff}}$, subject to a 'friction' term $(2/r)\,\mathrm{d}\phi/\mathrm{d}r$. Following the analysis in [6] and [12], we look for solutions to Equation 1.9 both inside and outside the spherical source. Inside the source, we can approximate the effective potential V_{eff} by

$$V_{\text{eff}}(\phi) \simeq \frac{\rho\phi^2}{2M^2} \tag{1.11}$$

when $\rho > \mu^2 M^2$. The interior solution is

$$\phi_{\text{in}}(r) \simeq C\frac{R}{r}\sinh\left(\frac{\sqrt{\rho}}{M}r\right) \tag{1.12}$$

for $r < R$, where R is the radius of the source and C is an undetermined constant. Outside the source, the symmetron evolves as a free field until it gets close to its minimum at $\phi = \phi_0$ [12]. We can therefore make the quadratic approximation

$$V_{\text{eff}}(\phi) = \frac{1}{2}m_0^2(\phi - \phi_0)^2, \tag{1.13}$$

and the exterior solution is given by

$$\phi_{\text{out}}(r) = D\frac{R}{r}\mathrm{e}^{-m_0(r-R)} + \phi_0 \tag{1.14}$$

where D is a second undetermined constant. By matching the field and its radial derivatives at $r = R$, the constants C and D are found to be

$$C = \phi_0\sqrt{\frac{\Delta R}{R}}\,\text{sech}\left(\sqrt{\frac{R}{\Delta R}}\right) \tag{1.15a}$$

$$\text{and } D = -\phi_0\left[1 - \sqrt{\frac{\Delta R}{R}}\tanh\left(\sqrt{\frac{R}{\Delta R}}\right)\right], \tag{1.15b}$$

where $\Delta R/R$ is the 'thin-shell factor':

$$\frac{\Delta R}{R} \equiv \frac{M}{\rho R^2} = \frac{M}{6M_{\text{Pl}}^2\Phi} = \frac{\phi_0}{6gM_{\text{Pl}}\Phi} \tag{1.16}$$

and $\Phi \equiv \rho R^2/6M_{\text{Pl}}^2$ is the gravitational potential of the source at its surface. To rewrite the thin-shell factor in terms of M_{Pl}, we have used the fact that if the symmetron force is to be comparable to gravity in a vacuum, we must impose that $\phi_0/M^2 \sim 1/M_{\text{Pl}}$, that is,

$$\phi_0 \equiv \frac{\mu}{\sqrt{\lambda}} = g\frac{M^2}{M_{\text{Pl}}} \tag{1.17}$$

where $g \sim \mathcal{O}(1)$. g measures the strength of the symmetron force on a test particle in a vacuum relative to gravity, such that $F_\phi = 2g^2F_{\text{N}}$. For a particle with $R \ll r \ll m_0^{-1}$, we can substitute the expression for D into the exterior solution, Equation 1.14. This results in an expression for the symmetron force on the particle relative to gravity:

$$\frac{F_\phi}{F_{\text{N}}} = -\frac{g}{M_{\text{Pl}}}\frac{\mathrm{d}\phi/\mathrm{d}r}{F_{\text{N}}} = 6g^2\frac{\Delta R}{R}\left[1 - \sqrt{\frac{\Delta R}{R}}\tanh\left(\sqrt{\frac{R}{\Delta R}}\right)\right]. \tag{1.18}$$

Objects that are screened have a small thin-shell factor, $\Delta R/R \ll 1$. This is due to the fact that a screened object will have relatively large gravitational potential Φ. The tanh

term in Equation 1.18 is therefore negligible for screened objects, and we have

$$\left.\frac{F_\phi}{F_\mathrm{N}}\right|_\mathrm{screened} \simeq 6g^2\frac{\Delta R}{R} \ll 1. \tag{1.19}$$

It is clear from Equation 1.19 that for screened objects, the small thin-shell factor causes the symmetron force on the particle relative to gravity to be heavily suppressed. A similar effect occurs in chameleon models [1]. For unscreened objects, the gravitational potential Φ is small such that the thin-shell factor is large: $\Delta R/R \gg 1$. In this case it makes sense to Taylor expand the tanh term, which leads to

$$\left.\frac{F_\phi}{F_\mathrm{N}}\right|_\mathrm{unscreened} \simeq 2g^2. \tag{1.20}$$

When $g \sim 1$, the symmetron will couple with gravitational strength to the source for objects that are unscreened. A coupling of this strength is promising with regards to the possibility of detecting the effects of new light scalar fields in experiment. In the next section, we discuss some existing constraints on the symmetron model from cosmological, laboratory and astrophysical tests.

1.4 Existing constraints on the symmetron model

1.4.1 Cosmological constraints

Screened light scalar fields that couple to matter such as the symmetron are good candidates for cosmological testing; provided the range of the fifth force is large enough and the coupling to matter is sufficiently strong, they naturally violate gravitational Solar System tests [38]. One such gravitational test is the test of general relativity carried out on the Cassini spacecraft [39]. By measuring the shift in frequency of radio photons to and from the Cassini probe as it passed near the Sun, the test was able to put a bound on how much gravity can be affected by other fields. In the symmetron model, the coupling of the scalar to matter is defined by

$$\beta(\phi_0) = \frac{M_\mathrm{Pl}\phi_0}{M^2} \tag{1.21}$$

where M_Pl is the Planck mass, ϕ_0 is the symmetron field and M is a mass scale. The results of the Cassini general relativity tests constrain this coupling as follows:

$$\beta(\phi_0)^2 \leq 4 \times 10^{-5} \tag{1.22}$$

where $\beta(\phi_0)^2$ is a measure of the strength of the fifth force acting on the Cassini probe. The above bound is valid as long as the range of the fifth force exceeds several astronomical units [38]. Assuming that the Cassini spacecraft is not screened but the Sun is screened, the constraint on $\beta(\phi_0)$ can be written as

$$\frac{\beta(\phi_0)\beta_\odot}{Z(\phi_0)} \leq 10^{-5} \tag{1.23}$$

where $\beta_\odot$ is the coupling between the scalar field and the Sun, and $Z(\phi_0)$ is a scaling factor. For the symmetron and other chameleon-like models, we can assume that $Z(\phi_0) = 1$ and $\beta(\phi_0) \simeq 1$, so the constraint on the coupling simplifies to

$$\beta_\odot \lesssim 10^{-5}, \tag{1.24}$$

which corresponds to the following bound on the value of the scalar field:

$$\phi_0 \lesssim 10^{-11}\ M_{\rm Pl}. \tag{1.25}$$

This bound is valid when we impose that the symmetron field vanishes in massive objects such as the Sun or planets.

Another class of cosmological tests able to constrain the symmetron is lunar laser ranging (LLR) experiments [40, 41]. These experiments measure the distance between the Earth and the Moon using laser ranging; a technique for determining distances by measuring the time taken for a laser pulse to return to the receiver. For the symmetron model, we assume that the scalar field value ϕ_0 is approximated by

$$\phi_0 \simeq \frac{\mu}{\sqrt{\lambda}}, \tag{1.26}$$

where μ is a mass scale and λ is a dimensionless coupling. The LLR bound is then

$$M \lesssim 10^{-3}\ M_{\rm Pl}, \tag{1.27}$$

where M is the mass scale in Equation 1.21. By comparison with Equation 1.24, we see that the LLR experiments constrain the symmetron even more strongly than the Cassini probe.

1.4.2 Laboratory tests

Casimir interaction and the Eöt–Wash experiment

In addition to cosmological tests, laboratory experiments are also able constrain light scalar field models such as the symmetron. One type of laboratory test that can be used to bound fifth forces is experiments investigating Casimir interaction. The Casimir effect is a phenomenon in quantum field theory in which the quantum fluctuations of a field result in a physical force that acts on some macroscopic boundaries of a confined space [42]. It manifests in experiments involving two conducting plates separated by some distance d. The magnitude of the classical pressure due to the scalar field between the plates is given by

$$\left|\frac{F_\phi}{A}\right| = V_{\rm eff}(\phi(0)) - V_{\rm eff}(\phi_0) \tag{1.28}$$

where F_ϕ is the force associated with the scalar field, A is the surface area of the conducting plates and $V_{\rm eff}$ is the effective potential. For the symmetron model, the value of $\phi(0)$ is very close to its vacuum value $\phi_0 \simeq \mu/\sqrt{\lambda}$ as long as the mass scale

$\mu \gtrsim d^{-1}$. This implies that $F_\phi/A \simeq 0$, that is, the Casimir effect will be negligible if the symmetron has a large mass in comparison to the inverse distance between the plates [38]. In the opposite scenario when $\mu \lesssim d^{-1}$, the symmetron field is close to zero both in and between the conducting plates [43], and the symmetron is decoupled from matter inside the experiment. In this case, the magnitude of the pressure due to the scalar field simplifies to

$$\left|\frac{F_\phi}{A}\right| = \frac{\mu^4}{4\lambda}. \tag{1.29}$$

The current strongest constraint on the intrinsic value of the Casimir pressure was obtained in a 2006 experiment by R. S. Decca and colleagues [44]:

$$\left|\frac{\Delta F_\phi}{A}\right| \leq 0.35 \text{ mPa}. \tag{1.30}$$

In some realistic tests of the Casimir pressure, including the work of Decca et al., the experimental set-up is composed of a plate and a sphere rather than two parallel plates. The bound in Equation 1.30 corresponds to a distance of $d = 746$ nm between the plate and the sphere, and a plate density on the order of $\rho_{\text{plate}} = 10 \text{ g cm}^{-3}$.

The Eöt–Wash experiment is similar to Casimir experiments, with the added complexity that the conducting plates are rotating rather than static [45]. Each of the rotating plates is drilled with a series of equally spaced holes arranged on a circle. As the plates rotate, the holes cause the gravitational and scalar interactions to become time-dependent, and a torque is induced between the plates. This torque is given by the rate of change of the potential energy due to the scalar force [46, 47]:

$$T \sim a_\theta \int_d^\infty \mathrm{d}x \frac{F_\phi}{A} \tag{1.31}$$

where θ is the angle of rotation of one plate relative to the other, and $a_\theta = \mathrm{d}A/\mathrm{d}\theta$ is a constant that depends only on the experimental parameters. For the symmetron model, the classical pressure arising from the torque between the two conducting plates is only non-zero when $d \lesssim \mu^{-1}$, where d is the distance between the plates and μ is a mass scale. We therefore have two distinct scenarios:

$$\begin{cases} T \simeq a_\theta \frac{\mu^4 d}{4\lambda} \text{ when } d \lesssim \mu^{-1} \\ T \simeq a_\theta \frac{\mu^3}{4\lambda} \text{ when } d \gtrsim \mu^{-1}, \end{cases} \tag{1.32}$$

that is, the torque increases linearly until it reaches some maximum value. According to the 2006 Eöt–Wash experiment [3], two conducting plates with a separation of $d = 55$ μd give the following bound on the torque:

$$|T| \leq a_\theta \Lambda_T^3, \tag{1.33}$$

where $\Lambda_T = 0.35\Lambda_{\text{DE}}$ and Λ_{DE} is characteristic of the energy scale associated with dark

energy, $\Lambda_{\rm DE} = 2.4$ meV [46].

Neutron bouncing experiments

It has been considered that new light scalar fields such as the chameleon and the symmetron could be detected via laboratory experiments involving bouncing ultracold neutrons [48, 49]. The experimental set-up consists of ultracold neutrons in the vicinity of a planar plate, which is acted on by Earth's gravitational field. The presence of a new scalar field can modify the energy levels of the bouncing neutrons. When the coupling of the scalar to nuclear matter is sufficiently strong, it is expected that the shift in the neutrons' energy levels will be detectable with sophisticated instruments such as the GRANIT spectrometer [50]. If the scalar field is a symmetron, the correction to the potential energy of the neutrons is dependent on

$$A(\phi) - 1 = \frac{\phi^2}{2M^2}, \tag{1.34}$$

where the symmetron field profile is defined by [51]

$$\phi(z) = \frac{\mu}{\sqrt{\lambda}} \tanh \frac{\mu z}{\sqrt{2}}. \tag{1.35}$$

The above equations are valid when we assume that the planar plate is completely screened. The shift in potential energy due to the symmetron field, δV, is bound by

$$|\delta E_3 - \delta E_1| \lesssim 2 \times 10^{-15} \text{ eV}, \tag{1.36}$$

where δE_3 and δE_1 are shifts in energy levels of the bouncing neutrons. We use this bound to inform our discussion on unexplored regions of parameter space in the symmetron model (see Figures 5.1 and 5.2).

Atom interferometry

Another type of laboratory test that has the potential to measure effects of a fifth force is experiments based on atom interferometry. These experiments are able to measure the acceleration of an atom in free fall very precisely [52, 53], and have been shown to be promising in searches for a classical fifth force F_ϕ [54, 55]. Atom interferometry involves placing a source mass at different positions in the vicinity of an atom. For each position of the source mass, the acceleration of the atom is measured. The experiment works on the basis that the presence of the source mass induces a non-vanishing field gradient associated with an unknown fifth force. The force between the source and the atom, $F_{\rm source}$, is then given by

$$F_{\rm source} = F_N + F_\phi, \tag{1.37}$$

where F_N is the Newtonian gravitational force acting on the atom, and F_ϕ is the fifth force. This fifth force is given by

$$F_\phi = -m_{\rm atom} \nabla \ln A(\phi), \tag{1.38}$$

where $m_{\rm atom}$ is the mass of the atom and $A(\phi)$ is the coupling function between the scalar field and matter. In theories involving screening, experimental tests using atom interferometry are of particular interest since small objects like atoms are usually unscreened [56, 57]. As a consequence of this, screened theories such as the symmetron model predict a large value of $F_{\rm source}$; that is, a measurable deviation from the Newtonian gravitational force. Atom interferometry experiments are generally performed inside vacuum chambers, on a distance scale on the order of cm. The strongest bounds on observable effects of the fifth force are found when the source mass is small, and inside the vacuum chamber [38]. Experiments with this set-up [54, 58, 59] have bound the acceleration between an atom and a marble-sized source to $a \lesssim 50$ nm s^{-2} when the distance between the atom and the source is $r \lesssim 1$ cm, which corresponds to strong constraints on the parameters of light scalar field models such as the chameleon and the symmetron [60]. We consider constraints on the symmetron model from atom interferometry further in Chapter 5 (see Figures 5.1 and 5.2).

Since the chameleon and symmetron theories are similar in many ways, the laboratory tests capable of putting constraints on each model overlap. However, one key difference between the two models is that the symmetron has a mass parameter μ, which causes it to be fixed to a length scale of μ^{-1}. The fifth force due to the symmetron field is exponentially suppressed when $L \gg \mu^{-1}$, where L is the length scale of the experiment. If instead we have $L \ll \mu^{-1}$, the symmetron field remains in its symmetric phase where $\phi = 0$, the symmetron decouples from matter and the fifth force vanishes. For this reason, we can conclude that a symmetron theory with a mass parameter μ must be experimentally tested on a length scale of $L \approx \mu^{-1}$, in order for observable effects to be a possibility.

Quantum constraints

In addition to the classical effects arising from the introduction of a new light scalar field, we expect that the vacuum fluctuations of these scalars will induce quantum interactions. The coupling of light scalar fields to matter and to the gauge bosons of the standard model is facilitated by the Higgs portal; that is, the coupling of the Higgs field to the scalar and to the standard model particles. It has been shown [61] that light scalar fields have an effect on quantities such as the fine structure constant, the mass of the Z boson and the Fermi interaction constant G_F. Precision tests of the standard model have put the following constraint on the mass scale M [61]:

$$M \gtrsim 10^3 \text{ GeV}. \tag{1.39}$$

Quantum interactions arising from light scalars can be measured in the laboratory; quantum effects occur in both Casimir and Eöt–Wash experiments, for example. Tests of the Casimir interaction can bound the quantum contributions to the pressure due to the scalar, F_x/A, and Eöt–Wash experiments bound the torque induced between the two rotating plates. For the symmetron model, the scalar field generally vanishes

everywhere when the mass parameter μ is less than $1/d$, where d is the distance between the conducting plates. This coincides with the vanishing of the linear coupling of the scalar field to matter, but the quadratic coupling, $A'' = 1/M^2$, remains; this term is the coupling to the quantum fluctuations. In the chameleon case, quantum effects are suppressed when the mass of the scalar becomes much lower than $1/d$ [62], and quantum constraints are therefore stronger in the symmetron model than in the chameleon model.

As a point of interest, we note that it has recently been shown that light scalar fields can explain one of the most prominent questions in modern-day particle physics: the anomalous magnetic moment of the muon [63]. Light scalar fields coupled to matter and photons induce a shift in the anomalous magnetic moment of charged particles. This shift occurs via two separate mechanisms: classically, the light scalar induces a change in the cyclotron frequency of the charged particles. Secondly, the scalar contributes to the anomalous magnetic moment at the quantum mechanical one-loop level. For light scalars without screening mechanisms, their contributions to the anomalous magnetic moment become negligible after applying the Cassini bound, and they therefore fail to resolve the anomaly. The screened theories of the chameleon and the symmetron, however, are both able to account for the anomalous magnetic moment without violating any known experimental constraints. For the symmetron model, the muon $g-2$ anomaly can be resolved when the following two bounds are satisfied [63]:

$$\frac{\mu^2}{2\lambda M^2} \lesssim 1 \tag{1.40a}$$

$$\text{and } \lambda \lesssim \frac{1}{6}. \tag{1.40b}$$

1.4.3 Astrophysical constraints

We now consider how astrophysical bodies such as stars, galaxies and galaxy clusters can be used in searches for a fifth force associated with a new light scalar field. In stars, the effects of the fifth force can be measured via the hydrostatic equilibrium equation, which is the condition on the pressure of the star which prevents it from collapsing under its own weight:

$$\frac{\mathrm{d}P}{\mathrm{d}r} = -\frac{G_N M(r)\rho(r)}{r^2}, \tag{1.41}$$

which is valid in the Newtonian limit of general relativity. The addition of a thin-shell-screened fifth force modifies the hydrostatic equilibrium equation to [38]

$$\frac{\mathrm{d}P}{\mathrm{d}r} = -\frac{G_N M(r)\rho(r)}{r^2}\left[1 + 2\beta^2\left(1 - \frac{M(r_s)}{M(r)}\right)\Theta(r - r_s)\right] \tag{1.42}$$

where $\Theta(x)$ is the Heaviside step function, β is the coupling coefficient of the scalar field and r_s is the screening radius of the star. The new light scalar field modifies gravity such that the inward gravitational force on the star is greater than Newtonian gravity alone; the star burns fuel at an increased rate and it is therefore brighter and shorter-lived.

This effect is more prominent in low-mass stars than in high-mass stars, and it also means that an unscreened galaxy would be more luminous and redder than a screened galaxy [38]. A numerical simulation of galaxy formation including fifth force effects could verify these predictions, although the complexity of such a simulation has thus far prevented these tests from being carried out.

In addition to stars, screened fifth forces can also affect the behaviour of galaxies. One such effect is the increase to a galaxy's rotation velocity and velocity dispersion, due to the additional force that arises from the scalar field. The symmetron model has been used to reproduce the radial acceleration relation, which correlates the observed and baryonic accelerations of galaxies [64, 65]. Another observable effect of the fifth force may be found in the diffuse gas in a low-mass galaxy; if the density is sufficiently low, this gas can be unscreened and therefore affected by the fifth force. One consequence of this is that the gas will rotate faster than if it was screened [66, 67].

The most stringent constraints from astrophysical tests using thin-shell screened scalar field models involve galaxy morphology; that is, the structural properties of galaxies. Fifth force effects can manifest in unscreened galaxies surrounded by additional structure. We can assume that a star inside an unscreened galaxy is screened, since main-sequence stars self-screen [38]. The star is therefore not acted on by any fifth-force field that the galaxy may be in. The gas and dark matter surrounding the star, however, will be unscreened and will feel the additional acceleration due to the fifth force, a_ϕ. This results in the gas and dark matter moving in front of the star in the direction corresponding to the fifth-force field. Another observable effect arising from this scenario is that the stellar disk can become warped, due to the potential gradient induced across it. Both of these effects, the offset between stars and surrounding gas and the warping of stellar disks, have been studied numerically using Bayesian forward models [68–70]. These models have placed strong constraints on the matter coupling coefficient of a thin-shell-screened scalar field, within the range of 0.3 – 8 Mpc [71].

1.5 Fifth force experiments with ultracold atoms

The idea that scalar domain walls can be detected via their impact on matter particle trajectories has been explored on cosmological [13], Solar System [72] and laboratory scales [73]. In this work, we are interested in laboratory-scale tests of the fifth force, and specifically those in which a particle experiment performed inside a vacuum chamber can produce observable effects of the force induced by a symmetron coupling to matter. Significant progress has already been made in simulations of this type of experiment, as detailed in sections 1.2 and 1.4.2. One promising avenue for these laboratory tests is the use of ultracold atoms. Ultracold neutrons have already been used in searches for chameleon fields [48, 49, 74, 75], and in numerical simulations of symmetron domain wall dynamics. Llinares and Brax [73] have proposed a method to stabilize domain walls formed via the symmetron mechanism using filaments, and to detect these domain walls

in one of two ways: either by measuring the deflection angle of a beam of ultracold neutrons off the wall, or through the time difference of the neutrons passing through the wall. Ultracold particles are advantageous in such an experiment since they are slow-moving; if the velocities of the neutrons are around 1 m s^{-1}, the deviations of their trajectories due to a symmetron fifth force will be macroscopic as long as the range of the fifth force is on the order of 0.1 mm [73].

We extend the analysis in ref. [73] by considering the parameters necessary for a realizable experiment that measures the impact of the symmetron fifth force on the trajectory of a matter particle. We plan to use state-of-the-art 3D printing technology [76] to manufacture a topologically-tailored vacuum chamber with the non-isotropic matter distribution that is required to pin a domain wall in place. In the following chapters, we detail the analytical background for our proposed experiment and present results of our finite element numerical simulation of the effects of the fifth force on a matter particle. In Chapter 2, we derive the equation of motion for the symmetron field and calculate reflection and transmission coefficients for a matter particle approaching a domain wall. In Chapter 3, we explain our experimental set-up, and describe the formation of domain walls via the Kibble–Zurek mechanism. Chapter 4 introduces the finite element code we use for our simulations, SELCIE [77], and the modifications required in order for SELCIE to solve for symmetron rather than chameleon fields. Chapter 5 contains the results of our numerical simulation of the motion of a matter particle in the presence of the symmetron field. In Chapter 6, we investigate the possibility that the symmetron field can couple to electromagnetism, and calculate some approximate numerical values for the reflection and transmisson coefficients of a domain wall coupled to a photon. In Chapter 7 we summarize our findings, and consider avenues for future work in the detection of fifth-force effects associated with the symmetron model.

Chapter 2

Light Scalar Fields & Domain Walls

2.1 Domain wall solution for the symmetron field

The equation of motion describing the symmetron field is highly nonlinear, and therefore very difficult to solve analytically except for in very simple scenarios. However, by making some assumptions we can show that the domain wall solution to the symmetron equation of motion takes the form of a tanh profile. The physical interpretation of this approximate solution is an infinitely thin and straight domain wall. Since we are interested in vacuum solutions, we approximate the source as pressureless such that $\rho = 0$. The pressureless approximation can be very good in experimental contexts; going from natural units back to physical units, pressure terms are suppressed by factors of $1/c^2$ compared to density terms, and nothing in our model is moving at relativistic speeds. It is possible that if the mass becomes so high that the Compton wavelength is short enough to see substructure in the material (that is, the Compton wavelength is on the same scale as the atomic structure of the material), the approximation that matter can be treated as a smooth continuous density profile can break down. The validity of this approximation would need to be checked on a case-by-case basis. We choose the symmetry-breaking potential V associated with the scalar field ϕ to be

$$V = -\frac{1}{2}\mu^2\phi^2 + \frac{1}{4}\lambda^2\phi^4 \tag{2.1}$$

where μ is a mass scale and λ is a dimensionless coupling. To find the value of ϕ that minimizes V, we differentiate V with respect to ϕ,

$$\frac{\partial V}{\partial \phi} = -\mu^2\phi + \lambda^2\phi^3, \tag{2.2}$$

and set the result to 0:

$$\begin{aligned} -\mu^2\phi_{\min} + \lambda^2\phi_{\min}^3 &= 0 \\ \Rightarrow \phi_{\min} &= \pm\frac{\mu}{\lambda}. \end{aligned} \tag{2.3}$$

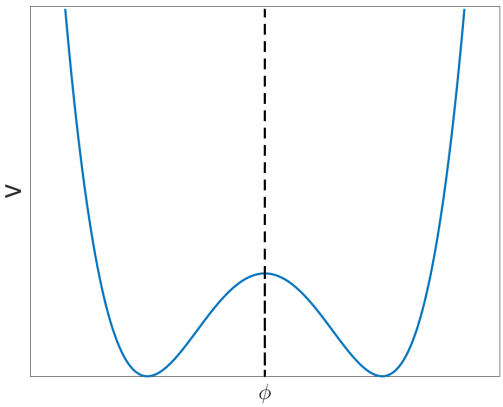

Figure 2.1: Plot of the symmetry-breaking potential in Equation 2.5 as a function of the scalar field ϕ. The dashed black line shows the location of the domain wall at $x = 0$.

Substituting $\phi = \phi_{\text{min}}$ into Equation 2.1 results in an expression for the minimum of the potential:

$$V_{\text{min}} = -\frac{\mu^4}{4\lambda^2}. \tag{2.4}$$

Cosmological implications of a large negative potential minimum are that present day vacuum energy is negative, which corresponds to a deceleration in the expansion of the Universe. We would therefore like to tune V_{min} to 0, so that there are no large-scale cosmological effects. We can achieve this by adding a term to the potential in Equation 2.1:

$$V = -\frac{1}{2}\mu^2\phi^2 + \frac{1}{4}\lambda^2\phi^4 + \frac{\mu^4}{4\lambda^2}. \tag{2.5}$$

This potential takes the form of a symmetric double well, as shown in Figure 2.1. Differentiation of Equation 2.5 with respect to ϕ shows that the value of ϕ_{min} remains the same as that of Equation 2.3. Substituting ϕ_{min} into Equation 2.5 gives the new value of V_{min}:

$$\begin{aligned} V_{\text{min}} &= \left(-\frac{1}{2}\mu^2\right) \times \left(\frac{\mu^2}{\lambda^2} + \frac{1}{4}\lambda^2\right) \times \left(\frac{\mu^4}{\lambda^4} + \frac{\mu^4}{4\lambda^2}\right) \\ &= -\frac{1}{2}\frac{\mu^4}{\lambda^2} + \frac{1}{2}\frac{\mu^4}{\lambda^2} \\ \Rightarrow V_{\text{min}} &= 0 \end{aligned} \tag{2.6}$$

as desired. The potential in Equation 2.5 can be written more simply in terms of ϕ_{min}. Consider

$$\begin{aligned} (\phi^2 - \phi_{\text{min}}^2)^2 &= (\phi^2 - \phi_{\text{min}}^2)(\phi^2 - \phi_{\text{min}}^2) \\ &= \phi^4 - 2\phi^2\phi_{\text{min}}^2 + \phi_{\text{min}}^4 \\ &= \phi^4 - 2\phi^2\frac{\mu^2}{\lambda^2} + \frac{\mu^4}{\lambda^4}. \end{aligned} \tag{2.7}$$

Multiplying the above expression by $\lambda^2/4$ results in

$$\begin{aligned}\frac{\lambda^2}{4}(\phi^2-\phi_{\text{min}}^2)^2 &= -\frac{1}{2}\mu^2\phi^2+\frac{1}{4}\lambda^2\phi^4+\frac{\mu^4}{4\lambda^2}\\ &= V\end{aligned} \tag{2.8}$$

and the potential V can therefore be written as

$$V=\frac{\lambda^2}{4}(\phi^2-\phi_{\text{min}}^2)^2. \tag{2.9}$$

The equation of motion of the scalar field ϕ is given by

$$\begin{aligned}-\frac{\mathrm{d}^2\phi}{\mathrm{d}x^2} &= -\frac{\mathrm{d}V}{\mathrm{d}\phi}\\ &= \frac{\mathrm{d}}{\mathrm{d}\phi}\left(\frac{\lambda^2}{4}(\phi^2-\phi_{\text{min}}^2)^2\right)\end{aligned} \tag{2.10}$$

where the first line is derived from the Euler–Lagrange equations. Let $y=\frac{\lambda^2}{4}(\phi^2-\phi_{\text{min}}^2)^2$ and $u=\phi^2-\phi_{\text{min}}^2$. Then $y=\frac{\lambda^2}{4}u^2$ and by the chain rule,

$$\begin{aligned}\frac{\mathrm{d}y}{\mathrm{d}\phi} &= \frac{\mathrm{d}y}{\mathrm{d}u}\frac{\mathrm{d}u}{\mathrm{d}\phi}\\ &= \frac{2\lambda^2}{4}u\times 2\phi=\lambda^2\phi u\\ &= \lambda^2\phi(\phi^2-\phi_{\text{min}}^2).\end{aligned} \tag{2.11}$$

The equation of motion for the scalar field ϕ is therefore

$$-\frac{\mathrm{d}^2\phi}{\mathrm{d}x^2}+\lambda^2\phi(\phi^2-\phi_{\text{min}}^2)=0. \tag{2.12}$$

Equation 2.12 is a second-order nonlinear differential equation. Nonlinear differential equations are notoriously difficult to solve, and are generally solved in one of two ways:

- Map the differential equation to an equation with a known solution.
- Solve the differential equation numerically.

For this reason, we will simply state the solution to Equation 2.12 here:

$$\phi(x)=\frac{\mu}{\lambda}\tanh\left(\frac{x}{\Delta}\right) \tag{2.13}$$

where

$$\Delta=\frac{\sqrt{2}}{\lambda\phi_{\text{min}}}. \tag{2.14}$$

Δ controls the width of the domain wall. The solution in Equation 2.13 is valid for two spacetime bubbles in different vacua, separated by a domain wall at $x=0$ as shown in

Figure 2.1. The boundary conditions for this solution are

$$\begin{cases} \phi = +\frac{\mu}{\lambda} \text{ when } x = +\infty \\ \phi = -\frac{\mu}{\lambda} \text{ when } x = -\infty. \end{cases} \tag{2.15}$$

We can prove that the tanh profile in Equation 2.13 is a solution by substituting it back into the equation of motion for ϕ (Equation 2.12). We begin by calculating the first term in the equation of motion, $-\mathrm{d}^2\phi/\mathrm{d}x^2$. Let $u = x/\Delta$ and then by the chain rule,

$$\begin{aligned} \frac{\mathrm{d}\phi}{\mathrm{d}x} &= \frac{\mathrm{d}\phi}{\mathrm{d}u}\frac{\mathrm{d}u}{\mathrm{d}x} \\ &= \frac{\mu}{\lambda}\operatorname{sech}^2\left(\frac{x}{\Delta}\right) \times \frac{1}{\Delta} \\ &= \frac{1}{\Delta}\frac{\mu}{\lambda}\operatorname{sech}^2\left(\frac{x}{\Delta}\right) \end{aligned} \tag{2.16}$$

where in the second line we have used the fact that $(\tanh(x))' = \operatorname{sech}^2(x)$. Now for the second derivative of ϕ with respect to x we have

$$\frac{\mathrm{d}^2\phi}{\mathrm{d}x^2} = \frac{\mathrm{d}}{\mathrm{d}x}\frac{\mathrm{d}\phi}{\mathrm{d}x} = \frac{\mathrm{d}}{\mathrm{d}x}\left(\frac{1}{\Delta}\frac{\mu}{\lambda}\operatorname{sech}^2\left(\frac{x}{\Delta}\right)\right) \tag{2.17}$$

Let $u = x/\Delta$ as before, $v = \operatorname{sech}(x/\Delta) = \operatorname{sech}(u)$ and

$$\begin{aligned} y &= \frac{1}{\Delta}\frac{\mu}{\lambda}\operatorname{sech}^2\left(\frac{x}{\Delta}\right) \\ &= \frac{1}{\Delta}\frac{\mu}{\lambda}v^2. \end{aligned} \tag{2.18}$$

By the chain rule,

$$\begin{aligned} \frac{\mathrm{d}y}{\mathrm{d}x} = \frac{\mathrm{d}y}{\mathrm{d}v}\frac{\mathrm{d}v}{\mathrm{d}x} &= \frac{\mathrm{d}y}{\mathrm{d}v}\frac{\mathrm{d}v}{\mathrm{d}u}\frac{\mathrm{d}u}{\mathrm{d}x} \\ &= \frac{2}{\Delta}\frac{\mu}{\lambda}v \times -\operatorname{sech}(u)\tanh(u) \times \frac{1}{\Delta} \\ &= -\frac{2}{\Delta^2}\frac{\mu}{\lambda}\operatorname{sech}^2\left(\frac{x}{\Delta}\right)\tanh\left(\frac{x}{\Delta}\right) \end{aligned} \tag{2.19}$$

where in the second line we have used the fact that $(\operatorname{sech}(x))' = -\operatorname{sech}(x)\tanh(x)$. The first term on the left hand side of Equation 2.12 is then

$$-\frac{\mathrm{d}^2\phi}{\mathrm{d}x^2} = \frac{2}{\Delta^2}\frac{\mu}{\lambda}\operatorname{sech}^2\left(\frac{x}{\Delta}\right)\tanh\left(\frac{x}{\Delta}\right). \tag{2.20}$$

Substituting Equations 2.13 and 2.20 into the equation of motion for ϕ (Equation 2.12) we find

$$\begin{aligned} \frac{2}{\Delta^2}\frac{\mu}{\lambda}\operatorname{sech}^2\left(\frac{x}{\Delta}\right)\tanh\left(\frac{x}{\Delta}\right) + \frac{\mu^3}{\lambda}\tanh^3\left(\frac{x}{\Delta}\right) \\ - \lambda\mu\tanh\left(\frac{x}{\Delta}\right)\phi_{\min}^2 = 0. \end{aligned} \tag{2.21}$$

Showing that the left hand side of the above equation does indeed vanish is sufficient proof that the tanh profile in Equation 2.13 is a solution to the equation of motion for the scalar field ϕ (Equation 2.12). Equation 2.21 can be simplified using the trigonometric identity $\operatorname{sech}^2(x) = 1 - \tanh^2(x)$:

$$\frac{2}{\Delta^2}\frac{\mu}{\lambda}\tanh\left(\frac{x}{\Delta}\right) - \frac{2}{\Delta^2}\frac{\mu}{\lambda}\tanh^3\left(\frac{x}{\Delta}\right) + \frac{\mu^3}{\lambda}\tanh^3\left(\frac{x}{\Delta}\right) - \lambda\mu\tanh\left(\frac{x}{\Delta}\right)\phi_{\min}^2 = 0. \tag{2.22}$$

$\phi_{\min} = \pm\mu/\lambda$ and $\Delta = \sqrt{2}/\lambda\phi_{\min}$, so we have

$$\phi_{\min}^2 = \frac{\mu^2}{\lambda^2} \tag{2.23a}$$

$$\Delta^2 = \frac{2}{\mu^2}. \tag{2.23b}$$

Substitution of Equations 2.23a and 2.23b into Equation 2.22 results in

$$\frac{\mu^3}{\lambda}\tanh\left(\frac{x}{\Delta}\right) - \frac{\mu^3}{\lambda}\tanh^3\left(\frac{x}{\Delta}\right) + \frac{\mu^3}{\lambda}\tanh^3\left(\frac{x}{\Delta}\right) - \frac{\mu^3}{\lambda}\tanh\left(\frac{x}{\Delta}\right) = 0$$
$$\Rightarrow 0 = 0. \tag{2.24}$$

We have shown that upon substitution of the tanh profile $\phi(x) = \mu/\lambda\tanh(x/\Delta)$ into the equation of motion for the scalar field ϕ (Equation 2.12), the left hand side does indeed vanish and the tanh profile is therefore a valid solution to the symmetron equation of motion.

2.2 1D symmetron field calculation

For our experiment to detect the scalar fifth force, we would like to manufacture some optimal matter distribution inside the vacuum chamber which would enable us to pin the domain walls to the chamber's interior. We therefore need to understand the behaviour of the symmetron field in the vacuum between two matter densities. To this end, it is useful to look at the vacuum solution to the symmetron equation of motion around two identical point sources in one spatial dimension. Simplifying the model in this way allows for a semi-analytical approach. In this section we follow the analysis in Section V of [78], where the density of the point sources is approximated by Dirac delta functions. This approximation is valid while the Compton wavelength of the symmetron field is much larger than the size of the sources [78]. We have two identical point sources of mass m, located at $\hat{x} = \pm\hat{x}_1$. The vacuum solution for the symmetron field around these two point sources is given in terms of Jacobi elliptic functions:

$$\varphi = \begin{cases} \varphi_0\,\mathrm{cd}\left(\frac{1}{\sqrt{2}}|\hat{x}|\sqrt{2-\varphi_0^2}, \frac{\varphi_0^2}{2-\varphi_0^2}\right) & |\hat{x}| < \hat{x}_1, \\ \tanh\left(\frac{1}{\sqrt{2}}\left(|\hat{x}| - \hat{x}_1\right) + \operatorname{arctanh}\varphi_1\right) & |\hat{x}| > \hat{x}_1 \end{cases} \tag{2.25}$$

where φ_0 is the field at $\hat{x} = 0$ (halfway between the point sources) and φ_1 is the field at $\hat{x} = \hat{x}_1$. φ_0 and φ_1 are constants that can be found by the solution of two simultaneous equations:

$$\varphi_1 = \varphi_0 \,\mathrm{cd}\left(\frac{1}{\sqrt{2}}\hat{x}_1\sqrt{2-\varphi_0^2}, \frac{\varphi_0^2}{2-\varphi_0^2}\right), \tag{2.26a}$$

$$\begin{aligned}\frac{m}{\mu M^2}\varphi_1 = {} & \frac{1}{\sqrt{2}}\left(1-\varphi_1^2\right) \\ & + \varphi_0 \frac{1-\varphi_0^2}{\sqrt{1-\frac{1}{2}\varphi_0^2}} \,\mathrm{nd}\left(\frac{\hat{x}_1}{\sqrt{2}}\sqrt{2-\varphi_0^2}, \frac{\varphi_0^2}{2-\varphi_0^2}\right) \mathrm{sd}\left(\frac{\hat{x}_1}{\sqrt{2}}\sqrt{2-\varphi_0^2}, \frac{\varphi_0^2}{2-\varphi_0^2}\right)\end{aligned} \tag{2.26b}$$

where $m/\mu M^2$ is a dimensionless combination of the mass scales μ and M. Since there is no known way to solve the above simultaneous equations analytically, we use Wolfram Mathematica® to determine φ_0 and φ_1, and plot the symmetron field profile given by Equation 2.25. Figure 2.2a shows the symmetron field profile for large particle separation, $\hat{x}_1 = \pi/2$. In this case, the point sources are seen by the symmetron field as two separate objects and the field has sufficient room to evolve towards its vacuum expectation value (the vacuum expectation value has been normalized to 1). The field profile is plotted for three different mass scales; as the mass m of the point sources increases, the field is pulled further from its vacuum expectation value. This is because in a large enough region of high density, the natural place for the normalized field to sit is 0 rather than 1. The case of small particle separation, $\hat{x}_1 = 0.1$, is shown in Figure 2.2b. When the particles are close together, the symmetron field is unable to distinguish between them; instead of two identical sources each of mass m, the field sees the sources as a single object of mass $2m$. The field does not have as much room to evolve towards its vacuum expectation value and thus stays approximately constant. In comparison with Figure 2.2a, the symmetron field is pushed further from its vacuum expectation value when the point source separation is small. Figure 2.2 is a reproduction of Figure 3 in [78].

The field profiles shown in Figure 2.2 give some useful insights into the behaviour of the symmetron field, but it would be interesting to explore this behaviour in more detail. It is unclear at present whether the transition between the two regimes in Figures 2.2a and 2.2b is smooth. As we linearly decrease the separation between the point sources, do we see linear behaviour in the symmetron field profile? In Figure 2.2b, is the field precisely flat in the centre of the point sources or is the curve just very shallow? These questions could be addressed with a more in-depth analysis of how the field profile changes as we modify the separation, $\hat{x}_1$, between the point sources.

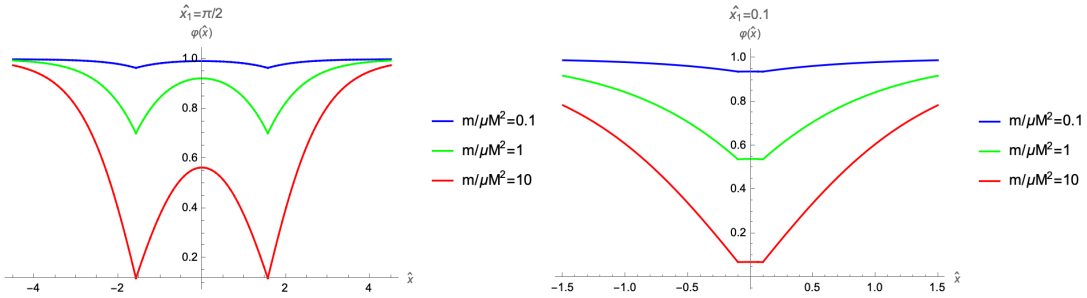

(a) Symmetron field profile for large particle separation, $\hat{x}_1 = \pi/2$. The field is plotted for three different mass scales.

(b) Symmetron field profile for small particle separation, $\hat{x}_1 = 0.1$. The field is plotted for three different mass scales.

Figure 2.2: Field profiles for the symmetron field around two identical point sources in one spatial dimension. These figures are a reproduction of Figure 3 in [78] using Wolfram Mathematica®.

2.3 Domain walls and reflection and transmission coefficients

2.3.1 Derivation of the wave equation for the matter field

We would like to design an experiment to detect the fifth force mediated by the symmetron field. As air is pumped out of a topologically-tailored vacuum chamber, topological defects (domain walls) will form and may be pinned to the interior of the chamber. A matter particle approaching one of these domain walls will feel the effects of the fifth force, and will be deflected or reflected off the domain wall. We first look at the simplified scenario in which a single matter particle is incident on a domain wall. We start with a Lagrangian for two scalar fields:

$$\mathcal{L} = -\frac{1}{2}\partial_\mu\phi\partial^\mu\phi - \frac{1}{2}\partial_\mu\chi\partial^\mu\chi - \frac{1}{2}m_\chi^2\chi^2 - \frac{1}{4}\lambda\left(\phi^2 - \eta^2\right)^2 - \frac{1}{2}\tilde{\lambda}\phi^2\chi^2 \tag{2.27}$$

where ϕ is the domain wall field and χ is the field of the matter particle. The third term in the above Lagrangian is the mass term for the matter particle, the fourth is the symmetry-breaking potential for the symmetron field ϕ, and the fifth is the interaction term (which allows the field of the particle χ to couple to that of the domain wall, ϕ). If the scalar field couples conformally to χ, then there should also be terms where ϕ multiplies the kinetic term for χ. However, the dominant impact of the coupling comes from the $\phi^2\chi^2$ term, and thus we are able to capture the important physics without these additional terms. We can use the Euler–Lagrange equations,

$$\frac{\partial\mathcal{L}}{\partial\phi} = \partial_\mu\left(\frac{\partial\mathcal{L}}{\partial\left(\partial_\mu\phi\right)}\right) \tag{2.28a}$$

$$\frac{\partial\mathcal{L}}{\partial\chi} = \partial_\mu\left(\frac{\partial\mathcal{L}}{\partial\left(\partial_\mu\chi\right)}\right), \tag{2.28b}$$

to derive the equations of motion for ϕ and χ. This leads to

$$\Box\phi - \lambda\phi\left(\phi^2 - \eta^2\right) - \tilde{\lambda}\phi\chi^2 = 0 \tag{2.29a}$$

$$\Box\chi - m_\chi^2\chi - \tilde{\lambda}\phi^2\chi = 0 \tag{2.29b}$$

where $\Box \equiv \partial^\mu\partial_\mu$ is the d'Alembert operator. We can now solve for the background domain wall, which requires the following assumptions:

1. $\chi = 0$ in the equation of motion for ϕ, Equation 2.29a.
2. The domain wall is static, so that time derivatives of ϕ vanish.

If we also assume that the domain wall is straight, that is, $\phi \equiv \phi(z)$, the equation of motion for ϕ reduces to

$$\frac{\mathrm{d}^2\phi}{\mathrm{d}z^2} = \lambda\phi\left(\phi^2 - \eta^2\right). \tag{2.30}$$

We showed in Section 2.1 that the solution to the above nonlinear differential equation is given by a tanh profile:

$$\phi(z) = \eta\tanh\left(\sqrt{\frac{\lambda}{2}}\eta z\right). \tag{2.31}$$

The next step in the derivation of a wave equation for the matter field χ is to add a χ wave on top of the domain wall background. Assuming that the wave is moving perpendicularly to the domain wall such that $\chi \equiv \chi(z,t)$, the equation of motion for χ (Equation 2.29b) reduces to

$$-\frac{\partial^2\chi}{\partial t^2} + \frac{\partial^2\chi}{\partial z^2} - m_\chi^2\chi - \tilde{\lambda}\phi^2\chi = 0. \tag{2.32}$$

Since Equation 2.32 is very similar to a wave equation, we can make the ansatz

$$\chi(z,t) = \hat{\chi}(z)\,\mathrm{e}^{-i\omega t}, \tag{2.33}$$

which results in

$$\hat{\chi}'' + \left(\omega^2 - m_\chi^2\right)\hat{\chi} - \tilde{\lambda}\phi^2\hat{\chi} = 0. \tag{2.34}$$

Substituting the tanh profile in Equation 2.31 into the above differential equation, we find

$$\begin{aligned}&\hat{\chi}'' + \left(\omega^2 - m_\chi^2 - \tilde{\lambda}\eta^2\right)\hat{\chi} + \tilde{\lambda}\eta^2\hat{\chi}\,\mathrm{sech}^2\sqrt{\frac{\lambda}{2}}\eta z = 0\\ &\Rightarrow \hat{\chi}'' + k_z^2\hat{\chi} + \tilde{\lambda}\eta^2\hat{\chi}\,\mathrm{sech}^2\sqrt{\frac{\lambda}{2}}\eta z = 0\end{aligned} \tag{2.35}$$

where in the second line we have rewritten $k_z^2 = \left(\omega^2 - m_\chi^2 - \tilde{\lambda}\eta^2\right)$ for simplicity. k_z can be thought of as a momentum. This equation is of the same form as the wave equation for the matter field χ given in Vilenkin and Shellard's book [13]. The wave equation for

χ can be simplified further if we approximate the domain wall as thin, that is,

$$\lim_{\alpha\to\infty} \frac{\alpha}{2} \operatorname{sech}^2(\alpha z) = \delta(z). \tag{2.36}$$

Since we always use finite values for the rest of the parameters, we never consider a scenario in which the domain wall can truly be described by a delta function. However, a delta function can be a very good approximation when the width of the domain wall is much smaller than the other length scales in the problem. Under this assumption, the wave equation for the matter field χ simplifies to

$$\hat{\chi}'' + k_z^2 \hat{\chi} + 2\sqrt{\frac{2}{\lambda}} \tilde{\lambda} \eta \delta(z) \hat{\chi} = 0. \tag{2.37}$$

Now that we have a wave equation for the matter field χ, we can use it to compute the reflection and transmission coefficients for a particle incident on a domain wall, and therefore the probability that a particle will be reflected off the domain wall.

2.3.2 Reflection and transmission coefficients

In Section 2.3.1, we derived the wave equation for the matter field χ incident on the domain wall (see Equation 2.37). We would like to find two separate solutions to Equation 2.37 for the left and the right of the domain wall, $z < 0$ and $z > 0$. $\delta(z) = 0$ everywhere apart from $z = 0$, so for both the left and right solutions the wave equation reduces to

$$\hat{\chi}'' + k_z^2 \hat{\chi} = 0. \tag{2.38}$$

The general solution to Equation 2.38 is

$$\begin{cases} \hat{\chi}_L = A\mathrm{e}^{ik_z z} + B\mathrm{e}^{-ik_z z} & z < 0 \\ \hat{\chi}_R = C\mathrm{e}^{ik_z z} & z > 0 \end{cases} \tag{2.39}$$

where $\hat{\chi}_L$ is the solution on the left of the wall ($z < 0$) and $\hat{\chi}_R$ is the solution on the right ($z > 0$). $A\mathrm{e}^{ik_z z}$ is the incident wave, $B\mathrm{e}^{-ik_z z}$ is the reflected wave and $C\mathrm{e}^{ik_z z}$ is the transmitted wave. The reflection and transmission coefficients for the particle are dependent on the amplitudes A, B and C. In order to obtain relations between these amplitudes, we can impose matching conditions on $\hat{\chi}$ and $\hat{\chi}'$ at the position of the wall ($z = 0$). $\hat{\chi}$ must be continuous across the boundary, such that $\hat{\chi}_L(0) = \hat{\chi}_R(0)$. This leads to

$$A + B = C. \tag{2.40}$$

The first derivative of the solution, $\hat{\chi}'$, is discontinuous across the domain wall by some amount that we will denote as Δ. To compute the size of the discontinuity in $\hat{\chi}'$, we can integrate Equation 2.37 over a very small region either side of the wall, from $-\epsilon$ to ϵ. Δ is then given by

$$\Delta = \hat{\chi}'_R(0) - \hat{\chi}'_L(0) = \int_{-\epsilon}^{\epsilon} \mathrm{d}z \hat{\chi}''. \tag{2.41}$$

Rearranging Equation 2.37 for $\hat{\chi}''$ and substituting into the equation for Δ we find

$$\begin{aligned}\Delta &= \int_{-\epsilon}^{\epsilon} \mathrm{d}z \left(-k_z^2 \hat{\chi} - 2\sqrt{\frac{2}{\lambda}} \tilde{\lambda} \eta \delta(z) \hat{\chi} \right) \\ &= -k_z^2 \int_{-\epsilon}^{\epsilon} \mathrm{d}z \hat{\chi} - 2 \int_{-\epsilon}^{\epsilon} \mathrm{d}z \sqrt{\frac{2}{\lambda}} \tilde{\lambda} \eta \delta(z) \hat{\chi} \\ &= -k_z^2 \int_{-\epsilon}^{\epsilon} \mathrm{d}z \hat{\chi} - 2\sqrt{\frac{2}{\lambda}} \tilde{\lambda} \eta \hat{\chi}(0) \end{aligned} \tag{2.42}$$

where we have used the sifting property of the delta function, $\int \mathrm{d}x f(x)\delta(x-a) = f(a)$, to evaluate the second integral. The first integral can be split up into two separate integrals on either side of the wall: from $-\epsilon$ to 0 (on the left of the wall) and from 0 to ϵ (on the right). We can then use the left and right solutions in Equation 2.39 to find an expression for Δ:

$$\begin{aligned}\Delta &= -k_z^2 \int_{-\epsilon}^{0} \mathrm{d}z \hat{\chi}_L - k_z^2 \int_0^{\epsilon} \mathrm{d}z \hat{\chi}_R - 2\sqrt{\frac{2}{\lambda}} \tilde{\lambda} \eta \hat{\chi}(0) \\ &= -k_z^2 \int_{-\epsilon}^{0} \mathrm{d}z (A\mathrm{e}^{ik_z z} + B\mathrm{e}^{-ik_z z}) - k_z^2 \int_0^{\epsilon} \mathrm{d}z C\mathrm{e}^{ik_z z} - 2\sqrt{\frac{2}{\lambda}} \tilde{\lambda} \eta \hat{\chi}(0) \\ &= -k_z^2 \left[\frac{A}{ik_z} \mathrm{e}^{ik_z z} - \frac{B}{ik_z} \mathrm{e}^{-ik_z z} \right]_{-\epsilon}^{0} - k_z^2 \left[\frac{C}{ik_z} \mathrm{e}^{ik_z z} \right]_0^{\epsilon} - 2\sqrt{\frac{2}{\lambda}} \tilde{\lambda} \eta \hat{\chi}(0) \\ &= -k_z^2 \left(\frac{A}{ik_z} - \frac{B}{ik_z} - \frac{A}{ik_z} \mathrm{e}^{-ik_z z} - \frac{B}{ik_z} \mathrm{e}^{ik_z z} \right) - kz^2 \left(\frac{C}{ik_z} \mathrm{e}^{ik_z z} - \frac{C}{ik_z} \right) - 2\sqrt{\frac{2}{\lambda}} \tilde{\lambda} \eta \hat{\chi}(0) \\ &= ik_z (A - B - A\mathrm{e}^{-ik_z z} + B\mathrm{e}^{ik_z z} + C\mathrm{e}^{ik_z z} - C) - 2\sqrt{\frac{2}{\lambda}} \tilde{\lambda} \eta \hat{\chi}(0). \end{aligned} \tag{2.43}$$

Using the relation $A + B = C$, the above equation simplifies to

$$\begin{aligned}\Delta &= ik_z (-A\mathrm{e}^{-ik_z z} + B\mathrm{e}^{ik_z z} + A\mathrm{e}^{ik_z z} + B\mathrm{e}^{ik_z z} - 2B) - 2\sqrt{\frac{2}{\lambda}} \tilde{\lambda} \eta \hat{\chi}(0) \\ &= ik_z \{ \mathrm{e}^{-ik_z z}(-A) + \mathrm{e}^{ik_z z}(A + 2B) - 2B \} - 2\sqrt{\frac{2}{\lambda}} \tilde{\lambda} \eta \hat{\chi}(0). \end{aligned} \tag{2.44}$$

We now impose that the region over which we have performed the integration, $-\epsilon$ to ϵ, is infinitely small. Taking the limit $\epsilon \to 0$ we find

$$\begin{aligned}\Delta &= ik_z(-A + A + 2B - 2B) - 2\sqrt{\frac{2}{\lambda}} \tilde{\lambda} \eta \hat{\chi}(0) \\ \Rightarrow \Delta &= -2\sqrt{\frac{2}{\lambda}} \tilde{\lambda} \eta \hat{\chi}(0). \end{aligned} \tag{2.45}$$

As can be seen in Equation 2.45, the first two integrals in the expression for Δ have disappeared and we are left with only the last term. In order to obtain a second equation involving the coefficients A, B and C, we must now rewrite $\hat{\chi}(0)$ in terms of these coefficients. We know that $\hat{\chi_L}$ and $\hat{\chi_R}$ must be equal at $z = 0$, that is, $\hat{\chi_L}(0) = \hat{\chi_R}(0)$.

From Equation 2.39 we have

$$\hat{\chi_L}(0) = A + B = \hat{\chi_R}(0) = C. \tag{2.46}$$

We can therefore say that $\hat{\chi}(0) = A + B$ and

$$\Delta = -2\sqrt{\frac{2}{\lambda}}\tilde{\lambda}\eta(A + B). \tag{2.47}$$

We can now use the first part of Equation 2.41 to eliminate Δ:

$$\begin{aligned}
\Delta &= \hat{\chi}'_R(0) - \hat{\chi}'_L(0) \\
&= ik_z C - ik_z A + ik_z B \\
&= ik_z A + ik_z B - ik_z A + ik_z B \\
\Rightarrow \Delta &= 2ik_z B
\end{aligned} \tag{2.48}$$

where in the third line we used the fact that $A + B = C$. Equating the two expressions for Δ we find

$$\begin{aligned}
2ik_z B &= -2\sqrt{\frac{2}{\lambda}}\tilde{\lambda}\eta(A + B) \\
\Rightarrow ik_z B + \sqrt{\frac{2}{\lambda}}\tilde{\lambda}\eta B &= -\sqrt{\frac{2}{\lambda}}\tilde{\lambda}\eta A \\
\Rightarrow \left(ik_z + \sqrt{\frac{2}{\lambda}}\tilde{\lambda}\eta\right) B &= -\sqrt{\frac{2}{\lambda}}\tilde{\lambda}\eta A.
\end{aligned} \tag{2.49}$$

We now have an equation relating the amplitude of the incident wave (A) to the amplitude of the reflected wave (B):

$$A = -\frac{ik_z + \sqrt{\frac{2}{\lambda}}\tilde{\lambda}\eta}{\sqrt{\frac{2}{\lambda}}\tilde{\lambda}\eta} B. \tag{2.50}$$

The reflection coefficient for the particle incident on the domain wall is defined as $R = |B|^2/|A|^2$, so from Equation 2.50 we have

$$\begin{aligned}
R = \frac{|B|^2}{|A|^2} &= \frac{|B|^2}{\left|-\frac{ik_z + \sqrt{\frac{2}{\lambda}}\tilde{\lambda}\eta}{\sqrt{\frac{2}{\lambda}}\tilde{\lambda}\eta} B\right|^2} \\
&= \frac{1}{\left|-\frac{ik_z + \sqrt{\frac{2}{\lambda}}\tilde{\lambda}\eta}{\sqrt{\frac{2}{\lambda}}\tilde{\lambda}\eta}\right|^2} \\
&= \frac{1}{\frac{\left(-ik_z + \sqrt{\frac{2}{\lambda}}\tilde{\lambda}\eta\right)\left(ik_z + \sqrt{\frac{2}{\lambda}}\tilde{\lambda}\eta\right)}{\frac{2}{\lambda}\tilde{\lambda}^2\eta^2}} \\
\Rightarrow R &= \frac{(2/\lambda)\tilde{\lambda}^2\eta^2}{k_z^2 + (2/\lambda)\tilde{\lambda}^2\eta^2}
\end{aligned} \tag{2.51}$$

where in the third line we used the fact that the squared modulus of any complex number z is $|z|^2 = z\bar{z}$. The reflection coefficient in Equation 2.51 can be written more simply if we let $\nu = 2(2/\lambda)^{1/2}\tilde{\lambda}\eta$, then $\nu^2 = 4(2/\lambda)\tilde{\lambda}^2\eta^2$ and

$$R = \frac{\nu^2}{4k_z^2 + \nu^2}. \tag{2.52}$$

In the limit of small k_z, we let $k_z \to 0$ which leads to $R \to 1$; this is the case of total reflection off the domain wall. Since k_z is related to the momentum of the incident particle, this behaviour makes physical sense; a particle with momentum below some threshold value does not have sufficient energy to traverse the domain wall and will be reflected back off it. In the limit of large k_z, we let $k_z \to \infty$ and then $R \to 0$; this is the case of no reflection. Particles with high momentum have enough energy to escape the potential well of the domain wall, and are able to travel straight through it. In addition to the reflection coefficient, we can now also calculate the transmission coefficient T, defined by $T = 1 - R$:

$$\begin{aligned} T = 1 - R &= 1 - \frac{\nu^2}{4k_z^2 + \nu^2} \\ \Rightarrow T &= \frac{4k_z^2}{4k_z^2 + \nu^2}. \end{aligned} \tag{2.53}$$

Equations 2.52 and 2.53 are identical to the reflection and transmission coefficients given in ref. [13]. Using the expressions for the reflection and transmission coefficients for the particle incident on the domain wall, it is possible to calculate the probability that the particle will be reflected off or transmitted through the domain wall. In the next chapter, we introduce our concept for a tabletop experiment that comprises a topologically-tailored vacuum chamber in which we can detect the effect of the symmetron fifth force on the trajectory of a matter particle.

Chapter 3

Vacuum Chamber Experiment

We propose an experiment comprised of a topologically-tailored vacuum chamber in which we can pin topological defects (domain walls) and detect the fifth force mediated by the symmetron field via deflection of a matter particle off a domain wall. Domain walls form inside the chamber as air is pumped out, and a symmetry-breaking phase transition occurs. The domain wall field is mediated by a scalar fifth force that interacts with matter; a matter particle incident on a domain wall will feel the effects of this fifth force and be deflected or reflected off the domain wall. In order for the deflection or reflection of the particle to be observed, the domain walls must be long-lived inside the vacuum chamber. It has been shown in [28] that it is possible to use structures inside the vacuum chamber to pin the domain walls in place, thus prolonging their lifetime and theoretically enabling the detection of matter particles deflected off them.

In order to maximize the lifetime of the domain walls and therefore also maximize the probability of observing the deflection of matter particles off the walls, it is important to consider the shape of the vacuum chamber's interior. A non-trivial vacuum chamber interior can be achieved in one of two ways; either with some structure that can be inserted into the chamber, or by manufacturing a vacuum chamber with a topologically-tailored interior. The latter method could make use of state-of-the-art 3D printing technology [76]. The purpose of this non-trivial matter distribution inside the chamber is to pin the domain walls in place and thus ensure that they are long-lived. It is not immediately clear what the optimal shape of the vacuum chamber interior would be. We start with an initial concept of two large spiked structures inside the chamber, between which a domain wall may be pinned. A simple illustration of this proposed geometry is shown in Figure 3.1. It is hoped that with careful consideration of the distribution of matter inside the chamber, we will be able to influence the domain wall dynamics such that it is long-lived, and deflection of a particle off the domain wall can be observed. This observation would constitute a clear experimental signature of the dark force.

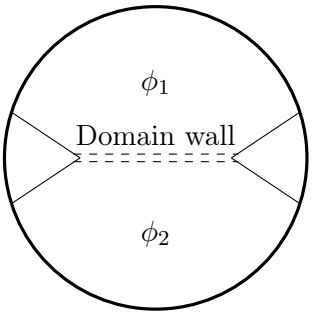

Figure 3.1: Simplified diagram showing a spherical vacuum chamber containing two spiked structures between which a domain wall may be pinned. ϕ_1 and ϕ_2 are two separate solutions for the symmetron field either side of the domain wall.

3.1 Formation of domain walls via the Kibble–Zurek mechanism

Mechanisms for the formation of topological defects due to symmetry breaking phase transitions were first studied quantitatively by Kibble in 1976 (ref. [21]). Kibble's theoretical framework was used by experimentalists in proposals for laboratory-based cosmological tests; notably Zurek in 1985 who suggested an analogue cryogenic experiment to test elements of the formation of cosmological strings [79]. To illustrate how domain walls form via the Kibble–Zurek mechanism, we consider a scalar field ϕ that has a discrete symmetry. This scalar field has a temperature-dependent effective potential $V_{\text{eff}}(\phi, T)$, and the following argument assumes that the mass of the scalar field is dependent on the temperature of the Universe rather than the density; the temperature acts as a proxy for the density ρ. When temperature dependence is taken into account, the effective potential of the scalar field is given by

$$V_{\text{eff}}(\phi, T) = V(\phi) + \frac{\lambda + 3e^2}{12} T^2 |\phi|^2 - \frac{2\pi^2}{45} T^4, \tag{3.1}$$

where the bare symmetron potential $V(\phi)$ is

$$V(\phi) = \frac{1}{4}\lambda(\phi^2 - \eta^2)^2, \tag{3.2}$$

and λ and η are positive constants. λ is equivalent to the coupling parameter of the symmetron model. Above a critical temperature T_c, the potential has a single minimum at $\phi = 0$. The critical temperature is defined by

$$T_c = \sqrt{6}\eta. \tag{3.3}$$

When the temperature drops below this critical value, a symmetry-breaking phase transition occurs and the potential develops two degenerate minima, as shown in Figure 3.2a. The scalar field ϕ can then roll into one or the other of these minima. We assume that ϕ will be subject to random fluctuations in different regions of space; these fluctuations cause the field to fall into one of the two ground states. If adjacent volumes of ϕ fall into opposite minima, a 'kink' solution forms as a boundary between the two

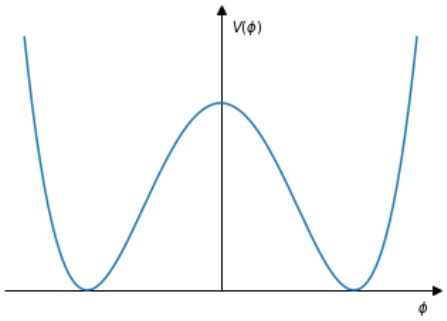

(a) The characteristic double-well potential of our scalar field theory. When the temperature drops below its critical value T_c, a symmetry-breaking phase transition occurs and the potential develops two degenerate minima.

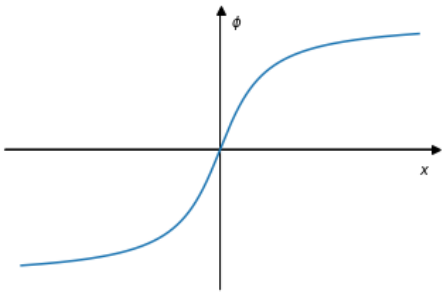

(b) The 'kink' solution that forms when two adjacent volumes of the scalar field ϕ fall into opposite minima.

Figure 3.2: The double-well potential in (a) gives rise to the 'kink' solution in (b), when adjacent volumes of ϕ fall into opposite minima.

volumes, as shown in Figure 3.2b. This boundary corresponds to what we refer to as a 'domain wall'.

Since we are interested in prolonging the lifetimes of domain walls, it is useful to study the dynamics of their formation in more detail. The critical temperature T_c on which the symmetry-breaking phase transition depends is related to a condition known as the Ginzburg criterion [80]:

$$\frac{|m(T)|}{\lambda T} \gg 1 \tag{3.4}$$

where T is the thermal energy and $m(T)$ is the effective mass of the scalar field. The Ginzburg temperature T_G is the temperature below the critical value T_c at which $|m(T_G)| \sim \lambda T_G$. As in ref. [13], we can use the form of the temperature-dependent effective potential to show that

$$T_c - T_G \sim \lambda T_c, \tag{3.5}$$

and therefore the Ginzburg temperature T_G is very close to the critical temperature T_c when $\lambda \ll 1$. In this case, the Ginzburg criterion in Equation 3.4 is satisfied everywhere except in a very narrow range of temperatures close to T_c. The physical consequence of falling below the Ginzburg temperature T_G is that temperature fluctuations in ϕ are not sufficient to lift the field from one minimum into the other; this scenario is called a 'freeze-out' [13]. When in a freeze-out state, the topological defects will persist rather than dissipate. The scale of the domain walls that form is determined by the correlation length ξ, which is defined to be the length scale above which the fluctuations in ϕ are uncorrelated. This means that the values of the scalar field ϕ in two regions of space are totally independent from one another if they are separated by a distance greater than ξ. The value of ξ depends nontrivially on on the dynamics of the phase transition, but we can constrain it with the simple causality bound:

$$\xi(t) < d_H(t) \tag{3.6}$$

where d_H is the causal horizon, which is defined to be the distance travelled by light during the lifetime of the Universe. This bound is a consequence of the fact that correlations cannot be formed faster than the speed of light. Formation of domain walls or networks of domain walls via the Kibble–Zurek mechanism can be described as a non-equilibrium phenomenon; the density of topological defects is exponentially suppressed at temperatures well below the critical temperature T_c. At such temperatures, the defects are able to survive since the field does not have sufficient time to reach equilibrium on scales greater than the correlation length ξ. When the temperature approaches T_c, the field is affected by thermal fluctuations that can allow it to surpass the potential barrier, which leads the topological defects to 'unwind'. In the case of an empty spherical vacuum chamber, we expect that any topological defects that form will tend to move out towards the chamber walls and dissipate, since the scalar field at the centre of the domain wall has the same value as in the physical walls of the vacuum chamber [60]. In order to be able to perform a particle experiment involving a domain wall, we must ensure that the domain wall does not immediately unwind after formation; to have the best chance of observing the effects of the fifth force on a matter particle, we would like to tailor the experimental scenario such that the domain wall is as long-lived as possible. In this proposed experiment, we exploit one key characteristic of the symmetron mechanism: in regions of very low density, the symmetron field can couple to matter with gravitational strength. Using this fact, we suggest a method by which domain walls are encouraged to form and their lifetimes can be extended: non-trivial vacuum chamber interiors, which can lead to the pinning of domain walls in place. We discuss how domain walls can be pinned to matter overdensities further in the context of our test particle simulation in Chapter 5.

3.2 Simple two-spike vacuum chamber model

As a first model, we propose a simple geometry made up of two dense spikes that protrude from the interior of the vacuum chamber, as illustrated in Figure 3.1. This interior structure could be achieved in various ways; by 3D printing the entire chamber, for example, or alternatively by printing an insert to be positioned inside the vacuum chamber. The rationale for starting with a model comprised of two protruding spikes is that it has been shown previously that domain walls formed via the symmetron mechanism can be pinned to matter overdensities [28]. Inside the dense regions, the symmetron field is decoupled and exhibits screening behaviour, so that its expectation value returns to zero. In our simple model, the two spikes on either side of the vacuum chamber are dense regions in which the symmetron field ϕ has a zero expectation value. If the distance between the two spikes is comparable to the correlation length ξ of the field, ϕ does not have enough space to reach equilibrium, or to roll into one of the two degenerate minima of the potential. In this scenario, the domain wall will be 'pinned' between the two spikes. The aim is to achieve pinning of the domain wall for a length of time such that experiments to investigate the interaction of matter particles with the domain wall can be carried out.

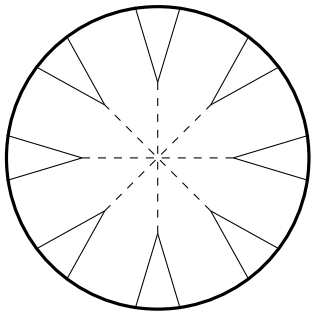

Figure 3.3: Simplified illustration of a vacuum chamber with a series of spikes protruding from the walls. Dashed lines indicate some possible locations where domain walls could form.

We choose this simple geometry as a proof of concept, and because it should allow the computational costs to remain relatively low in comparison with more complex interior geometries. However, an interesting area of further study is to implement a full optimization regime to find a configuration of matter inside the chamber that allows the domain walls to be as long-lived as possible within experimental constraints. One example of a more complex geometry is a series of spikes protruding from the chamber walls at various angles. If we can pin a domain wall between one pair of spikes, then we may be able to use a series of spikes to pin a network of domain walls inside the vacuum chamber, as illustrated in Figure 3.3. Since the formation of topological defects is a stochastic process, a greater number of spikes corresponds to a greater probability that a domain wall will be formed between at least one pair of spikes. In turn, the probability that at least one domain wall inside the chamber will be long-lived is increased. A long-lived domain wall corresponds to more time to perform particle experiments, and we are therefore more likely to be able to observe a deflection or reflection of a matter particle off a domain wall. In addition to the number of spikes, varying the thickness and separation of the spikes could also enable us to explore more of the symmetron parameter space.

3.3 Simulation of the two-spike model

To gain some insight into the experimental parameters required for a detection of the deflection or reflection of a matter particle off a domain wall, we simulate the simple model described in Section 3.2 numerically. The field equation describing the symmetron mechanism is highly nonlinear, and therefore very difficult to solve analytically. Using an open-source finite element software package called SELCIE [77], we can solve the static equation of motion for the symmetron. Once we have the static solution to the equation of motion, we can simulate the motion of a test particle on this background using an iterative method for the solution of differential equations called a 'leapfrog algorithm'. This allows us to investigate how the presence of a domain wall affects the test particle's motion. In Chapter 4, we describe in detail how the software package SELCIE works, and how it has been modified to solve for the scalar field theory that we

are interested in: the symmetron mechanism.

Chapter 4

SELCIE for the Symmetron

SELCIE (Screening Equations Linearly Constructed and Iteratively Evaluated) is a software package written in Python™ that uses the finite element method to find vacuum solutions for the chameleon field around a source with a user-defined mesh [77]. It uses the open-source finite element software FEniCS [81] in combination with two methods for the iterative solution of nonlinear differential equations: the Picard method and the Newton method. In this chapter, we show how we have modified the SELCIE code to solve for the symmetron field in addition to the chameleon. SELCIE uses the open-source 3D finite element mesh generation software Gmsh [82], with which the user may define the shape of their desired mesh with an arbitrary function. Figure 4.1 gives an example of how SELCIE can be used to solve for the chameleon field around an arbitrarily-shaped source. We use this capability to design vacuum chambers with interiors that are topologically-tailored to pin domain walls in place.

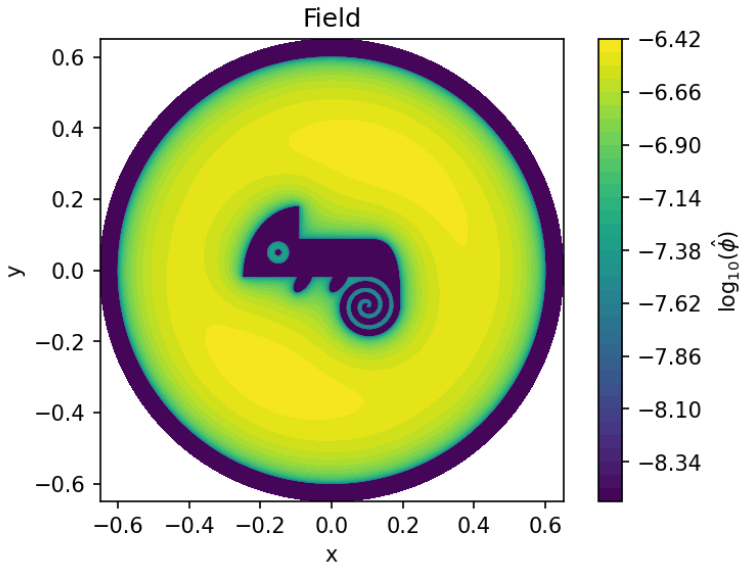

Figure 4.1: Example of SELCIE's user-defined mesh generating capabilities: the chameleon field solution is computed around the chameleon-shaped mass distribution inside a spherical vacuum chamber. The colour bar corresponds to $\log_{10}$ of the chameleon field $\hat{\phi}$. Image courtesy of Chad Briddon.

4.1 How does SELCIE work?

SELCIE is a software package based on the finite element method, which allows the user to construct an arbitrary system of mass distributions and then calculate the corresponding solution to the chameleon field equation [77]. As discussed in Chapter 1, the chameleon model is a light scalar field theory in which the mass of the scalar field is dependent on the local matter density. As the local matter density increases, the mass of the chameleon field also increases. In the symmetron mechanism, however, it is the expectation value of the scalar field that is dependent on the local matter density. In order to use SELCIE to find solutions for our chosen scalar field theory, the symmetron model, we have written a new solver to be used with the SELCIE code that finds the solution to the symmetron equation of motion rather than the chameleon equation of motion. SELCIE uses one of two methods for the solution of nonlinear differential equations: the Picard or the Newton method, in conjunction with the finite element method. The finite element solution is computed using the open-source FEniCS Project software [81]. The finite element method is chosen over the more commonly used finite difference method for the ease with which it can adapt to irregularly-spaced meshes; SELCIE is able to solve for the chameleon profile around any arbitrarily-shaped source. Although not utilized in this work, we note that SELCIE also has the capability for mesh optimization: additional refinement can be added to the mesh in regions where the field solution is of particular interest, while the mesh is made coarser in other regions. This allows the user to solve the field equation to a greater degree of accuracy without significantly increasing the computational cost.

In the finite element method, the domain of the problem Ω is divided into 'cells' that are defined by their vertices P_i. We can decompose the field $u(\underline{x})$ using the basis functions $e_i(\underline{x})$, such that

$$u(\underline{x}) = \sum_i U_i e_i(\underline{x}) \tag{4.1}$$

where $U_i = U(P_i)$. Both the Picard and Newton iterative methods for the solution of nonlinear differential equations are inbuilt in SELCIE. The field solution obtained by SELCIE will be the same regardless of whether the Picard or the Newton method is chosen. There are positives and negatives to each method, as outlined in ref. [77]. The Picard method was shown to perform the fastest and also to scale better with mesh size: as the number of cells in the mesh increases, the run time of the solver increases less than it would if the Newton method were to be chosen instead. For this reason, we choose to use the Picard method in our simulation of the symmetron field.

4.2 Modifying SELCIE for the symmetron

SELCIE was built to solve for the chameleon field, which is defined by the equation of motion

$$\nabla^2\phi = -\frac{n\Lambda^{n+4}}{\phi^{n+1}} + \frac{\beta\rho}{M_{\rm Pl}} \tag{4.2}$$

where Λ is a mass scale, n is an integer and β is a coupling parameter. We can choose to express the chameleon field equation as a linear equation for a vector whose elements are the values of the field at each vertex, as shown in ref. [77]. Written in this form, the chameleon equation of motion is given by

$$[\alpha\mathbf{M} + (n+1)\mathbf{B}_k]\hat{\mathbf{\Phi}} = (n+2)\mathbf{C}_k - \hat{\mathbf{P}} \tag{4.3}$$

where $\hat{\mathbf{\Phi}}$ is a vector comprising the values of the field $\hat{\phi}$ at each vertex. $\mathbf{B}_k$ and $\mathbf{C}_k$ are defined by

$$[\mathbf{B}_k]_{ij} = \int_\Omega \hat{\phi}_k^{-(n+2)} e_i v_j \, \mathrm{d}x \tag{4.4a}$$

$$[\mathbf{C}_k]_j = \int_\Omega \hat{\phi}_k^{-(n+1)} v_j \, \mathrm{d}x, \tag{4.4b}$$

where v_i and v_j are test functions, and e_i are the basis functions of the field. The density vector $\hat{\mathbf{P}}$ is defined by

$$\hat{\mathbf{P}}_i = \int_\Omega \hat{\rho}(x) v_i \, \mathrm{d}x. \tag{4.5}$$

The indices i and j are counting the vertices of the mesh, and k is the relaxation index. SELCIE employs a relaxation method to solve for the scalar field: the user inputs an initial guess, and the solution is then allowed to relax to something that better solves the equation of motion. $k = 1$ corresponds to one relaxation towards the final solution. In order to use SELCIE to solve for the symmetron field rather than for the chameleon, we must write a new solver to find the solution to the symmetron equation of motion. This solver will require the symmetron equation of motion to be input in the same form as Equation 4.3. To write the symmetron equation of motion in this way, we follow a

three-step process:

1. Rescale the symmetron equation of motion.
2. Write the symmetron equation of motion in integral form.
3. Write the integral version of the symmetron equation of motion as a linear matrix relation.

We outline this process in detail in Sections 4.2.1–4.2.3.

4.2.1 Rescaling the symmetron equation of motion

We start with the differential form of the symmetron equation of motion as given in ref. [73], and write it in its simplest form. The differential version of the symmetron equation of motion is [73]:

$$\nabla^2\phi = \left(\frac{\rho}{M^2} - \mu^2\right)\phi + \lambda\phi^3. \tag{4.6}$$

where ρ is the density of the medium, μ and M are mass scales which define the nature of the effective potential in the presence of matter, and λ is a dimensionless constant. In order to eliminate λ from the equation of motion, we introduce a new field variable $\hat{\phi} \equiv \phi/\phi_\infty$ where the ϕ_∞ are the extrema of the symmetron field [78]:

$$\phi_\infty = \sqrt{\frac{\rho_0}{\lambda M^2}\left(\hat{\mu}^2 - 1\right)} \tag{4.7}$$

and the mass scale μ has been rescaled such that

$$\hat{\mu}^2 = \frac{M^2}{\rho_0}\mu^2. \tag{4.8}$$

We also rewrite the Laplacian such that $\hat{\nabla}^2 \equiv L^2\nabla^2$ where L is the length scale of the vacuum chamber. Substituting these new definitions into Equation 4.6, we find

$$\alpha\hat{\nabla}^2\hat{\phi} = -\left(\hat{\mu}^2 - \hat{\rho}\right)\hat{\phi} + \left(\hat{\mu}^2 - 1\right)\hat{\phi}^3 \tag{4.9}$$

where $\hat{\rho} \equiv \rho/\rho_0$ and the dimensionless constant α is given by

$$\alpha = \frac{M^2}{L^2\rho_0}. \tag{4.10}$$

ρ_0 is a reference density, typically chosen to be the density of the vacuum gas.

4.2.2 Integral version of the symmetron equation of motion

Following on from the rescaling of the symmetron equation of motion, the next step in putting the equation of motion in a form that can be used with SELCIE is to write it in its integral form. Following the method in ref. [77], we multiply both sides of Equation

4.9 by a test function v_j,

$$\alpha\hat{\nabla}^2\hat{\phi}v_j = -\left(\hat{\mu}^2 - \hat{\rho}\right)\hat{\phi}v_j + \left(\hat{\mu}^2 - 1\right)\hat{\phi}^3 v_j, \tag{4.11}$$

and integrate over the domain Ω to find:

$$\alpha\int_\Omega \hat{\nabla}^2\hat{\phi}v_j \,\mathrm{d}x = -\int_\Omega \left(\hat{\mu}^2 - \hat{\rho}\right)\hat{\phi}v_j \,\mathrm{d}x + \int_\Omega \left(\hat{\mu}^2 - 1\right)\hat{\phi}^3 v_j \,\mathrm{d}x. \tag{4.12}$$

The left hand side of Equation 4.12 can be integrated by parts:

$$\begin{aligned}\alpha\int_\Omega \hat{\nabla}^2\hat{\phi}v_j \,\mathrm{d}x &= \alpha v_j\hat{\nabla}\hat{\phi} - \alpha\int_\Omega \hat{\nabla}\hat{\phi}\cdot\hat{\nabla}v_j \,\mathrm{d}x \\ &= -\alpha\int_\Omega \hat{\nabla}\hat{\phi}\cdot\hat{\nabla}v_j \,\mathrm{d}x\end{aligned} \tag{4.13}$$

where the boundary term goes to 0 since v_j vanishes on $\partial\Omega$ for all j. Substitution of Equation 4.13 into Equation 4.12 gives us the integral form of the rescaled symmetron equation of motion:

$$\alpha\int_\Omega \hat{\nabla}\hat{\phi}\cdot\hat{\nabla}v_j \,\mathrm{d}x = \int_\Omega \left(\hat{\mu}^2 - \hat{\rho}\right)\hat{\phi}v_j \,\mathrm{d}x - \left(\hat{\mu}^2 - 1\right)\int_\Omega \hat{\phi}^3 v_j \,\mathrm{d}x. \tag{4.14}$$

4.2.3 The symmetron equation of motion as a linear matrix relation

As discussed in Section 4.1, we choose to use the Picard method for the iterative solution of nonlinear differential equations to find the symmetron field. In the Picard method, we take the Taylor expansion of the nonlinear term in the equation of motion around some field $\hat{\phi}_k$ which is the kth estimate of the field $\hat{\phi}$. In the case of the symmetron, the nonlinear term is the final term in Equation 4.14. Since the $\hat{\phi}_k$ will be updated each time the Taylor expansion is performed, it is sufficient to only expand up to the term linear in $\hat{\phi}$. Taylor expanding $\hat{\phi}^3$ around $\hat{\phi}_k$ we find

$$\begin{aligned}\hat{\phi}^3 &\simeq \hat{\phi}_k^3 + 3\hat{\phi}_k^2\left(\hat{\phi} - \hat{\phi}_k\right) + \mathcal{O}\left(\hat{\phi} - \hat{\phi}_k\right)^2 \\ &\simeq 3\hat{\phi}_k^2\hat{\phi} - 2\hat{\phi}_k^3.\end{aligned} \tag{4.15}$$

Substitution of the last line of Equation 4.15 into the integral version of the symmetron equation of motion in Equation 4.14 leads to

$$\alpha\int_\Omega \hat{\nabla}\hat{\phi}\cdot\hat{\nabla}v_j \,\mathrm{d}x = \int_\Omega \left(\hat{\mu}^2 - \hat{\rho}\right)\hat{\phi}v_j \,\mathrm{d}x - \left(\hat{\mu}^2 - 1\right)\int_\Omega \left(3\hat{\phi}_k^2\hat{\phi} - 2\hat{\phi}_k^3\right)v_j \,\mathrm{d}x. \tag{4.16}$$

With the equation of motion in this form, that is, the left hand side bilinear in $\hat{\phi}$ and v_j, and the right hand side linear in v_j, FEniCS can be used to solve for the scalar field $\hat{\phi}$. This procedure is then iterated by setting $\hat{\phi}_{k+1} = \hat{\phi}$, and solving for the new $\hat{\phi}$. The iteration scheme is repeated while the condition $\left|\hat{\phi}_{k+1} - \hat{\phi}_k\right| > \delta$ is satisfied, where δ is some tolerance set by the user.

Following the method laid out in ref. [77] for the chameleon field, we write the integral version of the symmetron equation of motion (Equation 4.16) as a linear matrix relation,

$$\mathbf{MU} = \mathbf{b} \tag{4.17}$$

where $\mathbf{U}$ is a vector with elements U_i. As in Equation 4.1, we decompose the symmetron field $\hat{\phi}$ using the basis functions $\hat{e}_i$:

$$\hat{\phi} = \sum_i \hat{\Phi}_i \hat{e}_i \tag{4.18}$$

where $\hat{\Phi}_i = \hat{\Phi}(P_i)$. Let $\mathbf{M}$ be a matrix with elements

$$M_{ij} = \int_\Omega \hat{\nabla}\hat{e}_i \cdot \hat{\nabla} v_j \, \mathrm{d}x. \tag{4.19}$$

The left hand side of Equation 4.16 then becomes

$$\alpha \mathbf{M}\hat{\mathbf{\Phi}}. \tag{4.20}$$

Rewriting the terms on the right hand side of Equation 4.16 in terms of the basis functions $\hat{e}_i$, we have

$$\begin{aligned}\alpha \mathbf{M}\hat{\mathbf{\Phi}} = &\left[\int_\Omega \hat{\mu}^2 \cdot \hat{e}_i \cdot v_j dx\right] \hat{\Phi}_i - \left[\int_\Omega \hat{\rho} \cdot \hat{e}_i \cdot v_j dx\right] \hat{\Phi}_i \\ &- \left[\int_\Omega 3\hat{\phi}_k^2 \left(\hat{\mu}^2 - 1\right) \cdot \hat{e}_i \cdot v_j dx\right] \hat{\Phi}_i + 2\left(\hat{\mu}^2 - 1\right) \int_\Omega \hat{\phi}_k^3 v_j \, \mathrm{d}x.\end{aligned} \tag{4.21}$$

Now let $\mathbf{P}$ be a vector with elements

$$P_{ij} = \int_\Omega \hat{\rho} \cdot \hat{e}_i \cdot v_j \, \mathrm{d}x, \tag{4.22}$$

and define the matrix $\mathbf{B}_k$ and the vector $\mathbf{C}_k$ by

$$[B_k]_{ij} = \int_\Omega \hat{\phi}_k^2 \cdot \hat{e}_i \cdot v_j \, \mathrm{d}x \tag{4.23a}$$

$$[C_k]_j = \int_\Omega \hat{\phi}_k^3 \cdot v_j \, \mathrm{d}x. \tag{4.23b}$$

In terms of these matrices, the symmetron equation of motion is

$$\alpha \mathbf{M}\hat{\mathbf{\Phi}} = \hat{\mu}^2 \hat{\mathbf{\Phi}} - \mathbf{P}\hat{\mathbf{\Phi}} - 3\left(\hat{\mu}^2 - 1\right)\mathbf{B}_k \hat{\mathbf{\Phi}} + 2\left(\hat{\mu}^2 - 1\right)\mathbf{C}_k, \tag{4.24}$$

or more simply:

$$\left[\alpha \mathbf{M} + \mathbf{P} + 3\left(\hat{\mu}^2 - 1\right)\mathbf{B}_k - \hat{\mu}^2 \mathbb{I}\right] \hat{\mathbf{\Phi}} = 2\left(\hat{\mu}^2 - 1\right)\mathbf{C}_k \tag{4.25}$$

where $\mathbb{I}$ is the identity matrix. Equation 4.25 is a modification of Equation 4.3, which solves for the symmetron equation of motion rather than for the chameleon. Now that

we have the symmetron equation of motion written in matrix form, we can write a new solver to be used in conjunction with the SELCIE code that finds solutions for the symmetron field around an arbitrarily-shaped source.

4.3 Reliability checks for the SELCIE symmetron solver

Now that we have succeeded in writing a new solver in SELCIE to find solutions to the symmetron equation of motion, it is essential to perform tests on the new code to check that it is working as expected and producing reliable results. As a first model, we choose an empty vacuum chamber and investigate how the field changes as we vary some of the model parameters. For these simulations, the radius of the vacuum chamber is set to 1.

4.3.1 The effect of varying $\hat{\mu}$

The parameter $\hat{\mu}$ is a mass scale related to the Compton wavelength of the field, which is the characteristic scale over which the field likes to vary:

$$\mathcal{C} = \frac{1}{\hat{\mu}} \tag{4.26}$$

where $\mathcal{C}$ is the Compton wavelength. A large value of $\hat{\mu}$ corresponds to a small value of the Compton wavelength $\mathcal{C}$. In order to test the validity of the symmetron solver, we ran the solver for a range of $\hat{\mu}$ values to see whether it was producing results in accordance with our expectations. Since the radius of the vacuum chamber is set to $L = 1$, we expect that the symmetron field will be zero everywhere when $\hat{\mu} < 1$, when the Compton wavelength is longer than the radius of the vacuum chamber. A test run on the empty vacuum chamber model confirms that this is indeed the case.

Figure 4.2 shows the symmetron field $\hat{\phi}$ as a function of $\hat{r}$, the radial distance from the centre of the vacuum chamber. As expected, the field is at its highest point in the centre of the vacuum chamber when $\hat{r} = 0$, and it returns to $\hat{\phi} = 0$ in the walls of the vacuum chamber where $\hat{r} = 1$, where the density is highest. As the value of $\hat{\mu}$ gets closer and closer to 1, the symmetron field has more room to get to where it wants to be: at one of the two degenerate minima. If $\hat{\mu}$ gets too close to 1, however, we see no field profile. In our test simulation for the symmetron field solution in an empty vacuum chamber, we found that the field remains at 0 for values of $\hat{\mu} \leq 1.0004$.

4.3.2 The effect of varying α

In addition to investigating what happens when we vary the value of $\hat{\mu}$, we also ran a series of simulations with the empty vacuum chamber model with various values of the constant α to see what effect changing α has on the symmetron field profile. As defined in Section 4.2.1, α is a dimensionless constant given by

$$\alpha = \frac{M^2}{L^2 \rho_0} \tag{4.27}$$

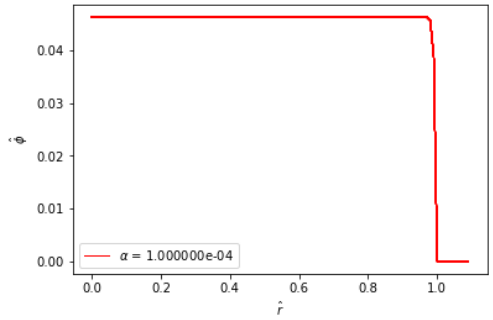

(a) The symmetron field $\hat{\phi}$ as a function of distance from the centre of the vacuum chamber $\hat{r}$, for $\hat{\mu} = 2$.

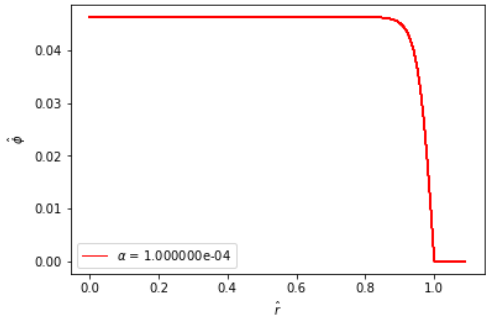

(b) The symmetron field $\hat{\phi}$ as a function of distance from the centre of the vacuum chamber $\hat{r}$, for $\hat{\mu} = 1.05$.

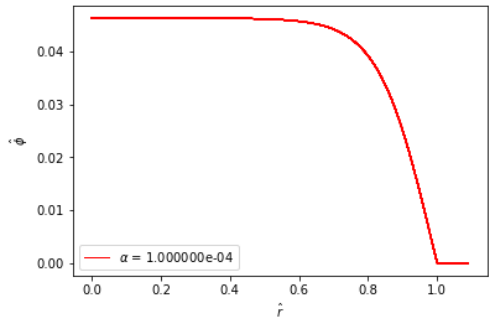

(c) The symmetron field $\hat{\phi}$ as a function of distance from the centre of the vacuum chamber $\hat{r}$, for $\hat{\mu} = 1.005$.

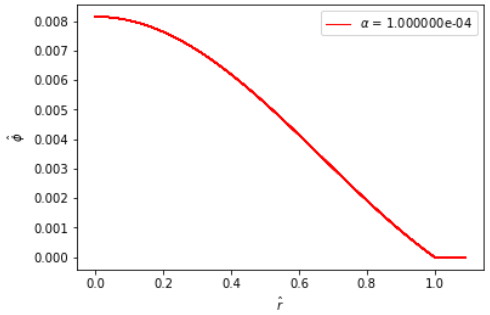

(d) The symmetron field $\hat{\phi}$ as a function of distance from the centre of the vacuum chamber $\hat{r}$, for $\hat{\mu} = 1.0005$.

Figure 4.2: The symmetron field $\hat{\phi}$ as a function of distance from the centre of the spherical vacuum chamber, $\hat{r}$, for a variety of $\hat{\mu}$ values. As the value of $\hat{\mu}$ gets closer to 1, the field has more room to reach one of the field minima.

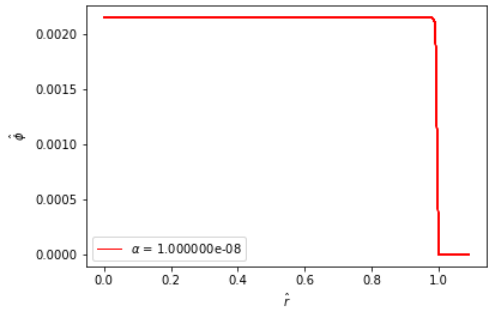

(a) The symmetron field $\hat{\phi}$ as a function of distance from the centre of the vacuum chamber $\hat{r}$, for $\alpha = 10^{-8}$.

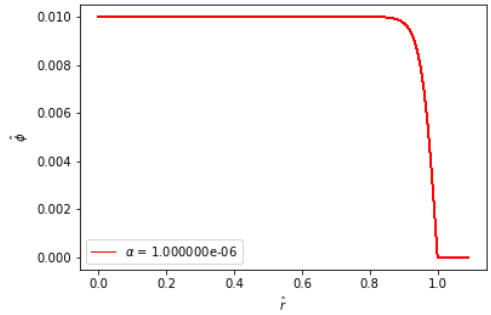

(b) The symmetron field $\hat{\phi}$ as a function of distance from the centre of the vacuum chamber $\hat{r}$, for $\alpha = 10^{-6}$.

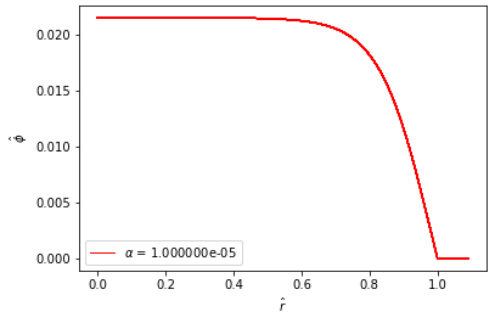

(c) The symmetron field $\hat{\phi}$ as a function of distance from the centre of the vacuum chamber $\hat{r}$, for $\alpha = 10^{-5}$.

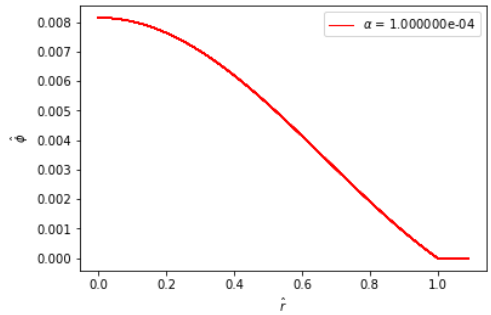

(d) The symmetron field $\hat{\phi}$ as a function of distance from the centre of the vacuum chamber $\hat{r}$, for $\alpha = 10^{-4}$.

Figure 4.3: The symmetron field $\hat{\phi}$ as a function of distance from the centre of the spherical vacuum chamber, $\hat{r}$, for a variety of α values. As the value of α increases, the field has more room to reach one of the field minima.

where M is a mass scale, L is the length of the vacuum chamber and ρ_0 is a reference density, typically taken to be the density of the vacuum gas. It appears as a scaling factor on the left hand side of the matrix representation of the symmetron equation of motion (Equation 4.25). We expect that, as was the case for $\hat{\mu}$, the symmetron field will be at its highest point in the centre of the vacuum chamber, and will go to zero in the chamber walls where the density is highest. The four panels in Figure 4.3 show that this is indeed the case. As the value of α increases, the symmetron field varies more slowly and it has more room to try to reach one of the two degenerate minima: this is the same effect as taking the value of the coupling parameter $\hat{\mu}$ closer to 1. Since the simulations for the empty vacuum chamber model agree with our expectations for what should happen to the symmetron field profile as we vary the parameters $\hat{\mu}$ and α, we can be reasonably confident that the symmetron solver for SELCIE is working correctly and producing reliable results.

4.4 Initial results with sources inside the chamber

4.4.1 Two-sphere model

After showing that the symmetron solver was working as expected, the next step is to use SELCIE's mesh-generating capabilities to design some vacuum chamber models with sources inside. As a first step, we choose a simple model with two identical spherical matter distributions inside the chamber. The results from this simulation are shown in Figure 4.4. We choose the values $\alpha = 10^{-10}$ and $\hat{\mu} = 100$ for this run of the code, since they correspond to a sharp field profile; the solution should be more defined than if the field were allowed to relax more slowly. The initial condition of the field is set to $\hat{\phi}_0 = 1$. The density distribution in 4.4a is chosen such that the density of matter in the chamber is zero everywhere apart from the two spherical sources. This is an idealized scenario: it would not be experimentally possible to achieve a density of exactly zero inside the chamber, although very low densities are achievable. A vacuum of 10^{-10} Torr of hydrogen, for example, corresponds to a vacuum density of $\rho_{\text{vac}} = 5 \times 10^{-35}$ GeV^4 (ref. [56]). Our idealized simulation should therefore give useful insight into the behaviour of the symmetron field solution around matter sources. Figure 4.4b shows the symmetron field solution obtained with the symmetron solver in SELCIE. The field is zero in the two spherical sources and in the vacuum chamber walls where the density is high, and it remains at one of the two degenerate minima in the rest of the chamber: $\hat{\phi} = 1$. In this case, a symmetry-breaking phase transition does not occur and we do not see the formation of a domain wall in the static field solution. The field profile in Figure 4.4c shows what we expect from the field solution: as we move radially outwards from the centre of the vacuum chamber at $\hat{r} = 0$ to the outer wall of the chamber at $\hat{r} = 1$, the field $\hat{\phi}$ is equal to 1 everywhere apart from in the spherical sources and in the chamber wall, where it is zero. Spiky features at the top of the field profile plot are numerical artefacts resulting from low mesh resolution; they appear around $\hat{\phi} = 1$ since this is a region in which the field solution is rapidly changing.

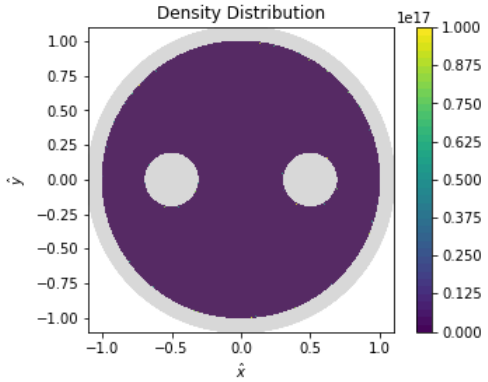

(a) Density distribution for the two-sphere model. The colour bar indicates the matter density inside the vacuum chamber.

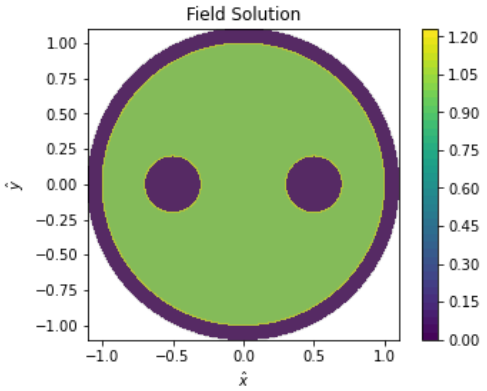

(b) Solution to the symmetron equation of motion obtained with the symmetron solver in SELCIE for the two-sphere model. The colour bar indicates the value of the symmetron field $\hat{\phi}$.

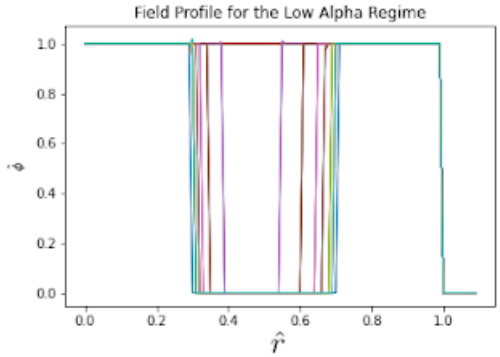

(c) Field profile showing the $\hat{r}$-dependence of $\hat{\phi}$ for the two-sphere model. Differently coloured lines correspond to different values of θ, the angle from the centre of the vacuum chamber to the outer wall.

Figure 4.4: Initial results from the symmetron solver with two identical spherical sources inside the vacuum chamber.

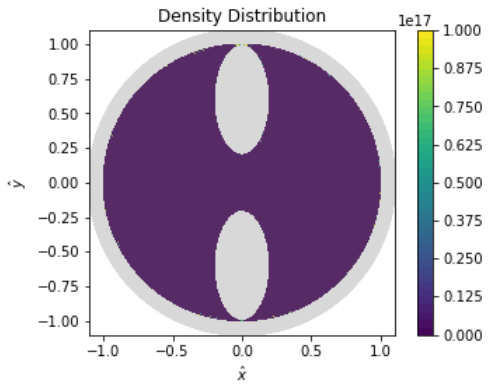

(a) Density distribution for the two-ellipse model. The colour bar indicates the matter density inside the vacuum chamber.

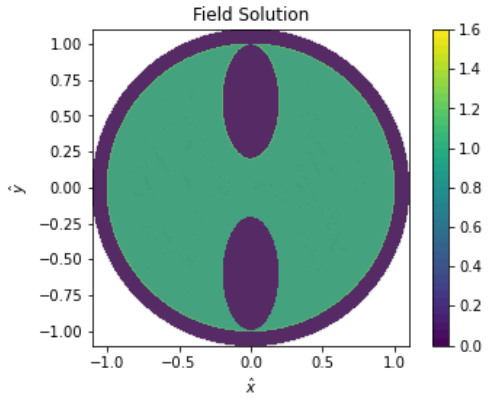

(b) Solution to the symmetron equation of motion obtained with the symmetron solver in SELCIE for the two-ellipse model. The colour bar indicates the value of the symmetron field $\hat{\phi}$.

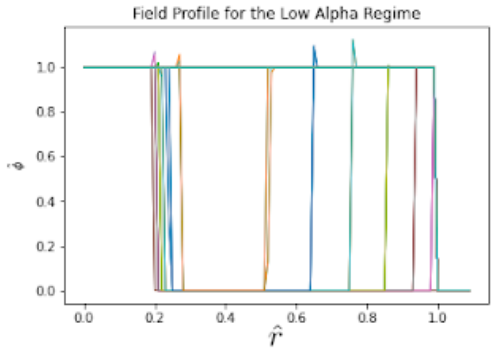

(c) Field profile showing the $\hat{r}$-dependence of $\hat{\phi}$ for the two-ellipse model. Differently coloured lines correspond to different values of θ, the angle from the centre of the vacuum chamber to the outer wall.

Figure 4.5: Initial results from the symmetron solver with two identical elliptical sources inside the vacuum chamber.

4.4.2 Two-ellipse model

As outlined in Section 3.2, our initial proposal for a topologically-tailored vacuum chamber is a simple model composed of two spikes which can pin a domain wall in place. We choose to make the sources elliptical rather than spherical, since ellipses are closer to our two-spike design. We can then use SELCIE's inbuilt mesh-generating function for ellipses to create a two-ellipse model. Figure 4.5 shows the results of a second test simulation of a model with two identical elliptical sources. To produce these results, we choose $\alpha = 10^{-10}$, $\hat{\mu} = 100$ and set the initial condition of the field as $\hat{\phi}_0 = 1$. As in the two-sphere model in Section 4.4.1, the density distribution is chosen such that the density of matter is zero everywhere apart from in the two elliptical sources, as shown in Figure 4.5a. Figure 4.5b shows the symmetron field solution calculated with the symmetron solver in SELCIE. The field is zero in the sources and in the vacuum chamber walls, and it remains at $\hat{\phi} = 1$ everywhere else in the chamber, as in the two-sphere model. The field does not have enough energy to escape from the potential well, and as

such there is no symmetry-breaking phase transition and a domain wall does not form. The profile in Figure 4.5c matches our expectations for the behaviour of the field: at the centre of the vacuum chamber where $\hat{r} = 0$, the symmetron field $\hat{\phi} = 1$. As we move radially outward from the centre of the chamber towards $\hat{r} = 1$, the symmetron field is zero everywhere apart from in the elliptical mass distributions and in the walls of the vacuum chamber. As in the two-sphere model, spiky features appear in the field profile around $\hat{\phi} = 1$. These are numerical artefacts caused by the fact that the symmetron field solution is changing rapidly in this region; they would disappear if we were to increase the mesh resolution.

4.4.3 Spatially-varying initial conditions

In Section 4.4.1, we showed that the symmetron solver for SELCIE produces physically sensible results for the symmetron field around two identical sources. However, we did not observe the formation of domain walls: we would like to investigate the regime where it is not energetically favourable for the field to return to $\hat{\phi} = 1$ in the region between the two sources. To see the formation of domain walls in our simulations, we may need to 'seed' the domain wall in the initial conditions of the field. One way of achieving this is to use a spatially-varying initial guess. We showed in Section 2.1 that the analytical solution for the symmetron field of an infinite and straight domain wall is given by a tanh profile:

$$\hat{\phi}(x) = \frac{\hat{\mu}}{\lambda} \tanh\left(\frac{x}{\Delta}\right) \tag{4.28}$$

where

$$\Delta = \frac{\sqrt{2}}{\lambda \phi_{\text{min}}}. \tag{4.29}$$

It therefore makes sense to try a spatially-varying initial guess that follows a tanh profile, to encourage a domain wall to form. We achieve this using SELCIE's inbuilt function for spatially-varying initial conditions. We choose to make the tanh profile very sharp, so that it approximates a step function. The reason for this is that when the initial condition is very sharp, we are making very few assumptions about how the field will behave. The initial field values in the two halves of the chamber are then $\hat{\phi}_0 = \pm 1$, that is, the two degenerate minima of the field.

Figure 4.6 shows the initial results of the two-ellipse model with a spatially-varying initial condition in the form of a tanh profile. We choose a value of $\hat{\mu}$ very close to 1 ($\hat{\mu} = 1.0000001$) for this simulation, since it is interesting to see what happens in the case of spatially-varying initial conditions when the field is allowed to relax more slowly. In Figure 4.6a it is clear that a symmetry-breaking transition has occurred: the field values in the two halves of the chamber are $\hat{\phi} = \pm 1$, and a domain wall has formed between the two ellipses along the $\hat{y} = 0$ axis. In each half of the chamber, the symmetron field has insufficient energy to escape from the potential well and it therefore remains at each of the two degenerate minima. The mesh patterns in both halves of the chamber are numerical artefacts which disappear when the mesh is more refined, at the cost of

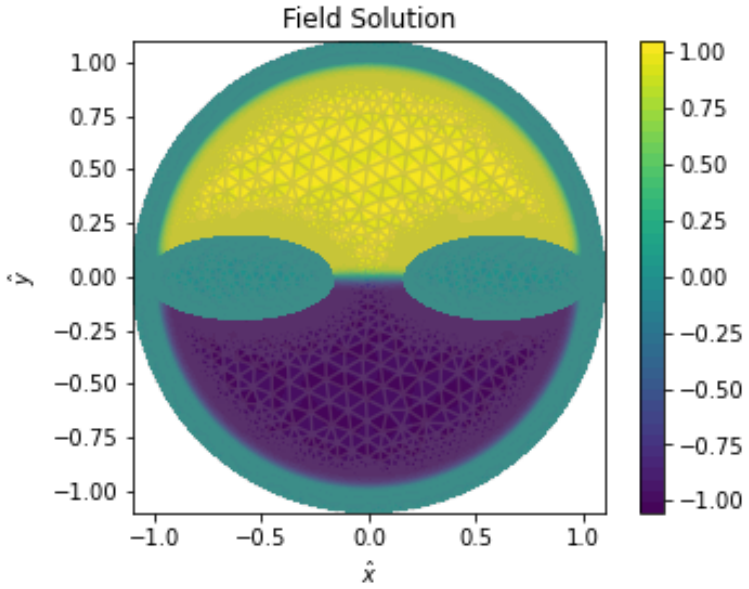

(a) Field solution for the two-ellipse model with a spatially-varying initial condition. The colour bar indicates the value of $\hat{\phi}$.

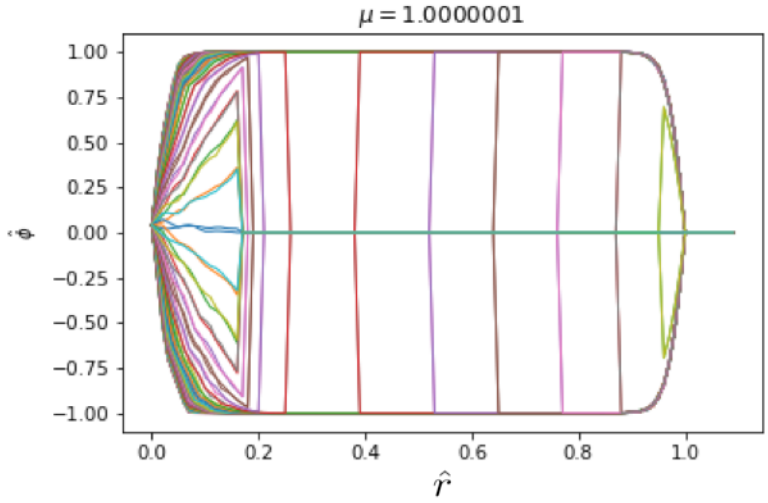

(b) Field profile for the two-ellipse model with a spatially-varying initial condition. Differently coloured lines correspond to different values of θ, the angle from the centre of the vacuum chamber to the outer wall.

Figure 4.6: Initial results obtained with the symmetron solver in SELCIE for the two-ellipse model with a spatially-varying initial condition.

increased computational time. We note that these spatially-varying initial conditions are extremely idealized, and it is possible for a domain wall form in this scenario without any sources inside the chamber; in some test runs of the code, we found that a domain wall can exist in an empty vacuum chamber. However, the presence of matter overdensities can encourage domain walls to form, and might allow us to ensure that a domain wall is longer-lived. Figure 4.6b shows the symmetron field profile as a function of $\hat{r}$, the radius of the vacuum chamber. As expected, as we move radially outwards from the centre of the chamber at $\hat{r} = 0$ to the outer wall at $\hat{r} = 1$, $\hat{\phi} = 0$ in the elliptical sources and in the chamber walls, and in the rest of the chamber $\hat{\phi} = \pm 1$ depending on which half of the chamber we are moving through.

We have shown that with a careful choice of parameters and initial conditions, we can encourage a domain wall to form in a topologically-tailored vacuum chamber. The next step is to use this static domain wall solution to perform simulations with test particles, in order to investigate the effect that a domain wall has on the motion of matter. In Chapter 5, we detail our results of test particle simulations on the static domain wall solution, and discuss their implications.

Chapter 5

Test Particle Simulation

In the presence of a domain wall, a matter particle will be acted upon by the fifth force proportional to the scalar gradient arising from the formation of the wall. If the new light scalar field originates from a modification of gravity, then we might expect the scalar to couple universally to gravity. If the scalar comes from particle physics then this universal coupling might be an approximation, but the differences between couplings to different particle species are generally expected to be small [83]. If we can pin a domain wall in place inside a vacuum chamber as described in Chapter 3, we can then perform a particle experiment to detect the effect that the domain wall has on the motion of matter. A deflection of a matter particle by a domain wall would constitute a clear experimental signature of the fifth force. In realistic experiments, the matter particles used could be ultracold atoms or molecules, or nanobeads. We simulate a simple experimental scenario in which a test particle is dropped with some initial velocity towards the pinned domain wall. We can make some predictions for the behaviour of the particle using the analytic solution for an infinite and straight domain wall. How well the experimental results are modelled by the analytic solution will vary depending on the thickness of the domain wall.

5.1 Infinite and straight domain walls

The equation of motion of an infinite, straight and static domain wall is solved by a tanh profile:

$$\phi(y) = \phi_0 \tanh\left(y/d\right) \tag{5.1}$$

where $d = \sqrt{2}/\mu$ is the width of the domain wall, and

$$\phi_0^2 = \frac{\mu^2}{\lambda}\left(1 - \frac{\rho_0}{\rho_*}\right). \tag{5.2}$$

As in ref. [73], we can use conservation of energy arguments to make analytical predictions for the behaviour of a test particle in the presence of an infinite and straight domain wall. We assume that the test particle couples to the scalar field in the same way that the matter sourcing the scalar field profile does. In each direction, the conserved Hamiltonian

of a test particle of unit mass is given by [73]

$$H_y = \frac{\dot{y}^2}{2} + \frac{\phi^2(y) - \phi_0^2}{2M^2}, \tag{5.3}$$

where we have chosen the zero point of the Hamiltonian to lie at infinity. Rearranging the Hamiltonian in terms of the particle velocity $\dot{y} = \frac{\mathrm{d}y}{\mathrm{d}t}$, we find

$$\frac{\mathrm{d}y}{\mathrm{d}t} = \left(2H_y - \frac{\phi^2(y) - \phi_0^2}{M^2}\right)^{1/2} \tag{5.4}$$

$$= \left(2H_y - \frac{\phi_0^2 \tanh^2(y/d) - \phi_0^2}{M^2}\right)^{1/2} \tag{5.5}$$

where in the second line we have used the tanh profile solution in Equation 5.1. To solve for the particle's position y, we rewrite the above equation as

$$\int_{y_0}^{y} \frac{1}{\left(2H_y - \frac{\phi_0^2 \tanh^2(y/d) - \phi_0^2}{M^2}\right)^{1/2}} \,\mathrm{d}y = \int_{t_0}^{t} \mathrm{d}t \tag{5.6}$$

$$\Rightarrow \int_{y_0}^{y} \frac{1}{(2H_y)^{1/2}\left(1 - \frac{\phi_0^2}{2H_y M^2}\tanh^2(y/d) + \frac{\phi_0^2}{2H_y M^2}\right)^{1/2}} \,\mathrm{d}y = t - t_0. \tag{5.7}$$

We now introduce the quantity $1 + \phi_0^2/(2H_y M^2)$, which we call a^2 when positive and $-\alpha^2$ when negative:

$$\begin{cases} a^2 = 1 + \phi_0^2/(2H_y M^2) > 0 \\ -\alpha^2 = 1 + \phi_0^2/(2H_y M^2) < 0. \end{cases} \tag{5.8}$$

In the positive case, we have

$$\frac{\phi_0^2}{2H_y M^2} = a^2 - 1 \tag{5.9}$$

and the left hand side of Equation 5.7 becomes

$$\frac{1}{(2H_y)^{1/2}} \int_{y_0}^{y} \frac{1}{(1 - (a^2-1)(\tanh^2(y/d) - 1))^{1/2}} \,\mathrm{d}y. \tag{5.10}$$

Using the identity $\tanh^2(x) = 1 - \mathrm{sech}^2(x)$, this simplifies to

$$\frac{1}{(2H_y)^{1/2}} \int_{y_0}^{y} \frac{1}{(1 - (a^2-1)\,\mathrm{sech}^2(y/d))^{1/2}} \,\mathrm{d}y \tag{5.11}$$

or

$$\frac{1}{(2H_y)^{1/2}} \int_{y_0}^{y} \frac{1}{\left(1+\frac{a^2-1}{\cosh^2(y/d)}\right)^{1/2}}\,\mathrm{d}y. \tag{5.12}$$

This integral can be solved by substitution. We choose

$$u = \frac{\sinh(y/d)}{a} \tag{5.13}$$

$$\Rightarrow \frac{\mathrm{d}u}{\mathrm{d}y} = \frac{\cosh(y/d)}{ad}, \tag{5.14}$$

so that the integral becomes

$$\frac{1}{(2H_y)^{1/2}} \int_{\frac{1}{a}\sinh(y_0/d)}^{\frac{1}{a}\sinh(y/d)} \frac{1}{\left(1+\frac{a^2-1}{\cosh^2(y/d)}\right)^{1/2}} \frac{ad}{\cosh(y/d)}\,\mathrm{d}u, \tag{5.15}$$

which can be rewritten as

$$\frac{1}{(2H_y)^{1/2}} \int_{\frac{1}{a}\sinh(y_0/d)}^{\frac{1}{a}\sinh(y/d)} \frac{1}{\left(1+\frac{a^2-1}{1+\sinh^2(y/d)}\right)^{1/2}} \frac{ad}{(1+\sinh^2(y/d))^{1/2}}\,\mathrm{d}u. \tag{5.16}$$

Equation 5.13 can be rearranged as

$$\sinh(y/d) = au, \tag{5.17a}$$

$$\sinh^2(y/d) = a^2u^2. \tag{5.17b}$$

Substituting these expressions into Equation 5.16 results in the simplified integral

$$\frac{d}{(2H_y)^{1/2}} \int_{\frac{1}{a}\sinh(y_0/d)}^{\frac{1}{a}\sinh(y/d)} \frac{1}{(u^2+1)^{1/2}}\,\mathrm{d}u. \tag{5.18}$$

We may now use the standard integral

$$\int \frac{1}{(x^2+A^2)^{1/2}} = \operatorname{arcsinh}\left(\frac{x}{A}\right) + C \tag{5.19}$$

to find

$$\frac{d}{(2H_y)^{1/2}} \left(\operatorname{arcsinh}\left(\frac{1}{a}\sinh(y/d)\right) - \operatorname{arcsinh}\left(\frac{1}{a}\sinh(y_0/d)\right)\right) = t - t_0 \tag{5.20}$$

where we have substituted back in the right hand side of Equation 5.7. Rearranging and taking sinh of both sides results in an expression describing one type of behaviour exhibited by the test particle:

$$\sinh\left(\frac{y(t)}{d}\right) = a\sinh\left(\frac{(2H_y)^{1/2}(t-t_0)}{d} + \operatorname{arcsinh}\left(\frac{\sinh\left(y_0/d\right)}{a}\right)\right). \tag{5.21}$$

Equation 5.21 is valid when the quantity $a^2 = 1 + \phi_0^2/(2H_yM^2) > 0$, and it describes the scenario in which a test particle passes through the domain wall.

To find an expression for the second type of behaviour exhibited by a test particle, we return to the integral in Equation 5.6:

$$\int_{y_0}^{y} \frac{1}{\left(2H_y - \frac{\phi_0^2\tanh^2(y/d)-\phi_0^2}{M^2}\right)^{1/2}}\,\mathrm{d}y = t - t_0. \tag{5.22}$$

Using the identity $\tanh^2(x) = 1 - \operatorname{sech}^2(x)$, we can rewrite the integral on the left hand side as

$$\frac{1}{(-2H_y)^{1/2}}\int_{y_0}^{y} \frac{1}{\left(-1 - \frac{\phi_0^2}{2H_yM^2}\operatorname{sech}^2(y/d)\right)^{1/2}}\,\mathrm{d}y. \tag{5.23}$$

In the negative case in Equation 5.8 we have $\alpha^2 = -[1 + \phi_0^2/(2H_yM^2)] > 0$, such that

$$-\frac{\phi_0^2}{2H_yM^2} = \alpha^2 + 1. \tag{5.24}$$

Substituting this into Equation 5.23, we find

$$\frac{1}{(-2H_y)^{1/2}}\int_{y_0}^{y} \frac{1}{(-1 + (\alpha^2+1)\operatorname{sech}^2(y/d))^{1/2}}\,\mathrm{d}y \tag{5.25}$$

$$= \frac{1}{(-2H_y)^{1/2}}\int_{y_0}^{y} \frac{1}{\left(-1 + \frac{\alpha^2+1}{\cosh^2(y/d)}\right)^{1/2}}\,\mathrm{d}y \tag{5.26}$$

$$= \frac{1}{(-2H_y)^{1/2}}\int_{y_0}^{y} \frac{1}{\left(-1 + \frac{\alpha^2+1}{1+\sinh^2(y/d)}\right)^{1/2}}\,\mathrm{d}y \tag{5.27}$$

where we have used the additional trigonometric identities $\operatorname{sech}^2(x) = 1/\cosh^2(x)$ and

$\cosh^2(x) = 1 + \sinh^2(x)$. To solve this integral, we make the substitution

$$u = \frac{\sinh(y/d)}{\alpha} \tag{5.28}$$

$$\Rightarrow \frac{\mathrm{d}u}{\mathrm{d}y} = \frac{\cosh(y/d)}{\alpha d}, \tag{5.29}$$

and the integral becomes

$$\frac{1}{(-2H_y)^{1/2}} \int_{\frac{1}{\alpha}\sinh(y_0/d)}^{\frac{1}{\alpha}\sinh(y/d)} \frac{1}{\left(-1 + \frac{\alpha^2+1}{1+\sinh^2(y/d)}\right)^{1/2}} \frac{\alpha d}{\cosh(y/d)}\,\mathrm{d}u \tag{5.30}$$

$$= \frac{1}{(-2H_y)^{1/2}} \int_{\frac{1}{\alpha}\sinh(y_0/d)}^{\frac{1}{\alpha}\sinh(y/d)} \frac{1}{\left(-1 + \frac{\alpha^2+1}{1+\sinh^2(y/d)}\right)^{1/2}} \frac{\alpha d}{(1+\sinh^2(y/d))^{1/2}}\,\mathrm{d}u \tag{5.31}$$

where in the second line we have used the fact that $\cosh(x) = (1 + \sinh^2(x))^{1/2}$. Rearranging the equation for u we find

$$\sinh(y/d) = \alpha u, \tag{5.32a}$$

$$\sinh^2(y/d) = \alpha^2 u^2, \tag{5.32b}$$

and the integral in Equation 5.31 simplifies to

$$\frac{d}{(-2H_y)^{1/2}} \int_{\frac{1}{\alpha}\sinh(y_0/d)}^{\frac{1}{\alpha}\sinh(y/d)} \frac{1}{(1-u^2)^{1/2}}\,\mathrm{d}u. \tag{5.33}$$

We may now use the standard integral

$$\int \frac{1}{(A^2 - x^2)^{1/2}}\,\mathrm{d}x = \arcsin\left(\frac{x}{A}\right) + C \tag{5.34}$$

to find

$$\frac{d}{(-2H_y)^{1/2}} \left(\arcsin\left(\frac{1}{\alpha\sinh(y/d)}\right) - \arcsin\left(\frac{1}{\alpha\sinh(y_0/d)}\right)\right) = t - t_0 \tag{5.35}$$

where we have substituted back in the right hand side of Equation 5.22. Rearranging this expression and taking sin of both sides results in

$$\sinh\left(\frac{y(t)}{d}\right) = \alpha \sin\left(\frac{(-2H_y)^{1/2}(t-t_0)}{d} + \arcsin\left(\frac{\sinh(y_0/d)}{\alpha}\right)\right). \tag{5.36}$$

Equation 5.36 is valid when the quantity $\alpha^2 = -[1 + \phi_0^2/(2H_y M^2)] > 0$, and it describes the scenario in which the test particle is trapped in the potential well of the domain wall.

To summarize: we find that in the presence of a domain wall, the test particle will behave in one of two ways:

1. If $a^2 = 1 + \phi_0^2/(2H_y M^2) > 0$, the particle passes through the domain wall and

$$\sinh\left(\frac{y(t)}{d}\right) = a \sinh\left(\frac{(2H_y)^{1/2}(t-t_0)}{d} + \operatorname{arcsinh}\left(\frac{\sinh(y_0/d)}{a}\right)\right), \tag{5.37}$$

2. If $\alpha^2 = -[1 + \phi_0^2/(2H_y M^2)] > 0$, the particle gets trapped by the domain wall and

$$\sinh\left(\frac{y(t)}{d}\right) = \alpha \sin\left(\frac{(-2H_y)^{1/2}(t-t_0)}{d} + \arcsin\left(\frac{\sinh(y_0/d)}{\alpha}\right)\right) \tag{5.38}$$

where $y_0 = y(t_0)$ and $\dot{y}_0 = \dot{y}(t_0)$. The conserved Hamiltonian H_y is dependent on the velocity of the particle, and the behaviour of the particle in the presence of the domain wall is therefore determined by its velocity. Above some threshold initial velocity, the particle has enough energy to escape the potential well of the domain wall and travel through it, but slow-moving particles will get trapped by the domain wall and oscillate forwards and backwards across it.

5.2 Unexplored parameter space

Figure 5.1 shows the parameter space for our scalar field theory, where we have taken $\lambda = 10^{-10}$. By choosing a small value of λ, we are compromising between what is natural and what is phenomenologically interesting: one might argue that natural values of λ are much larger. However, we are focusing in on a region of parameter space in which observable effects are possible in experiment. Very small values of λ are motivated by pheonomenology such as gravitational waves; domain walls can source the observed stochastic gravitational-wave background when [34]

$$\frac{\mu}{\lambda^{1/3}} \approx 10^5 \text{ GeV}, \tag{5.39}$$

which could correspond to values of λ much smaller than 10^{-10}. For this reason, we also consider constraints on the symmetron model when $\lambda = 10^{-30}$ (see Figure 5.2). In both Figure 5.1 and Figure 5.2, the light opaque regions indicate where domain walls would not form within our idealized experiment. The opaque band on the right of each plot is the region in which the width of the domain walls would be greater than the size of the vacuum chamber. The triangular opaque regions correspond to when the density in the vacuum chamber walls is not high enough to restore the symmetry; for a domain wall solution, we require that the symmetry is broken in the gas but restored in the chamber walls. If figures 5.1 and 5.2 were larger, we would see an additional opaque band at the

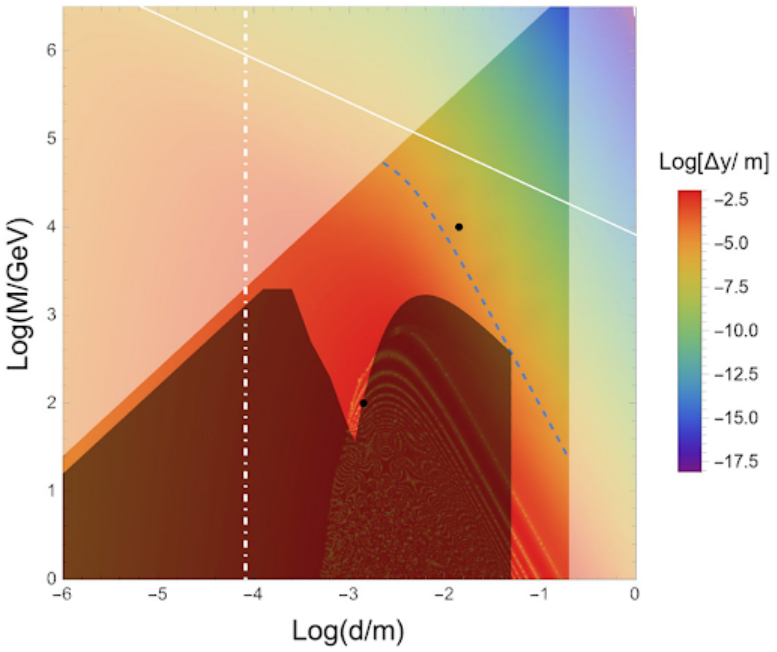

Figure 5.1: The parameter space for the scalar field theory, with $\lambda = 10^{-10}$ [84]. The light opaque shaded region indicates where domain walls would not form within our idealized experiment, and the dark opaque shaded region at the bottom of the plot is excluded by existing constraints from neutron bouncing experiments, cold neutron interferometry [85] and atom interferometry [59]. The black dots indicate two points of interest in the parameter space, corresponding to a thinner domain wall of width $d = 10^{-4}$ m and a thicker domain wall of width $d = 10^{-3}$ m.

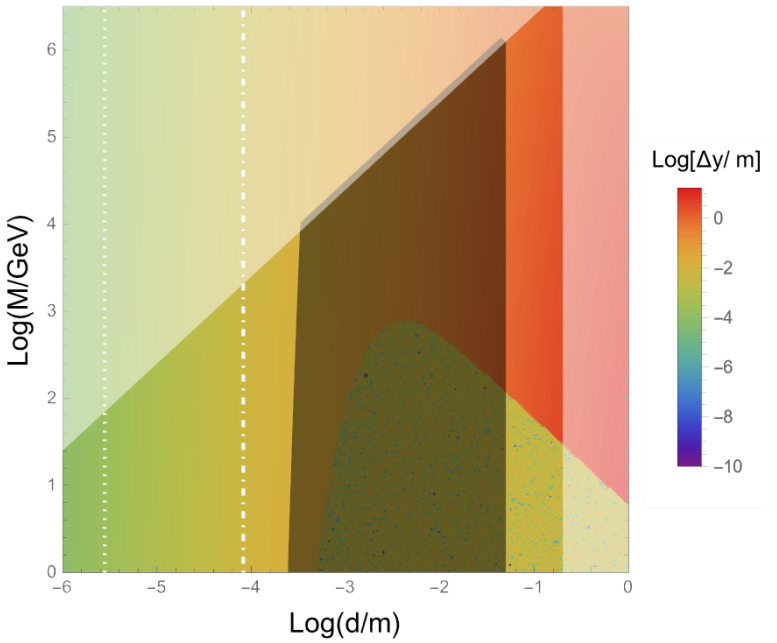

Figure 5.2: The parameter space for the scalar field theory, with $\lambda = 10^{-30}$ [84]. The light opaque shaded region indicates where domain walls would not form within our idealized experiment, and the dark opaque shaded region is excluded by existing constraints from atom interferometry [59].

bottom of each plot corresponding to the region in which the gas inside the vacuum chamber restores the symmetry. In both figures, the colour scale is $\Delta y = y(t) - y_0 + \dot{y}_0(t)$: the perturbation caused by a domain wall to the motion of a test particle after 10 s, with initial velocity $\dot{y}_0 = 10^{-3}$ m s^{-1} and starting position $y_0 = 5 \times 10^{-3}$ m, that moves perpendicularly towards an infinite straight domain wall located at $y = 0$. We choose this velocity because the equations in Section 5.1 describing the two types of behaviour of the test particle suggest that a particle of this initial velocity could exhibit the oscillatory motion in case 2 (Equation 5.38). Smaller values of λ correspond to stronger fifth forces, and therefore larger particle displacements. For obvious reasons, it is advantageous for the particle displacements to be as large as possible in experiments: a modern high precision camera is able to detect a displacement of $\Delta y = 10$ μm or more. The white dash–dotted line in both plots corresponds to $d = 8.2 \times 10^{-5}$ m, where quantum corrections from the symmetron field could play the role of the cosmological constant [63, 86].

In Figure 5.1, the dark opaque shaded region at the bottom of the plot is excluded by existing constraints from neutron bouncing experiments, cold neutron interferometry [85] and atom interferometry [59]. The curved lines towards the bottom right of Figure 5.1 correspond to the experimental scenario in which a particle is trapped in the potential well of the domain wall and undergoes sinusoidal oscillations, as in case 2 in Section 5.1. The dashed blue line indicates where $\Delta y = 10$ μm, which is the limit of current detectability. The white solid line shows where $\mu M_{\rm Pl} = \sqrt{\lambda} M^2$, that is, where the fifth force in vacuum has gravitational strength. The black dots in Figure 5.1 are two points of interest in the parameter space, which we explore in more detail in the rest of this chapter. They correspond to a thinner domain wall of width $d = 10^{-4}$ m, and a thicker domain wall of width $d = 10^{-3}$ m. Thin domain walls are more difficult to model numerically, since they require a much finer mesh for the solution of the scalar field. However, it is useful to examine the case of a thin domain wall for the purposes of comparison with our analytic solution for infinite and straight domain walls. If the numerical solution for a thin domain wall matches what we expect from the analytical calculation, this will be a good indication that the finite element code is working correctly. It is also useful to look at the case of a thicker domain wall, as this scenario is more easily achievable experimentally, and will give some insight into the particle deflections we can expect to achieve in a realistic experiment.

In Figure 5.2, the dark shaded region is excluded by existing constraints from atom interferometry [59]. Constraints from neutron bouncing experiments and cold neutron interferometry are not present in this plot, as these experiments are not relevant for the parameter space of $\lambda = 10^{-30}$. The curved region at the bottom right of the plot shows where a particle would be trapped in the potential well of the domain wall and undergo sinusoidal oscillations, as in case 2 in Section 5.1. Unlike in Figure 5.1, the details of these oscillations are not resolved. The white dotted line indicates where $\mu/\lambda^{1/3} = \text{MeV}$; close to this line, domain walls can make up a fraction of the dark matter in the Universe

today [11].

5.3 Evolving the motion of a test particle

Since infinite straight domain walls are not possible in any experimental scenario, we require a numerical solution to investigate the behaviour of a test particle in the presence of the domain wall. We use a leapfrog algorithm to evolve the motion of the particle on the static scalar field background. The leapfrog algorithm consists of an initial desynchronization of the velocity:

$$v_{1/2} = v - \frac{1}{2} a \mathrm{d}t \tag{5.40}$$

where a is the acceleration of the particle due to the symmetron field. In terms of the gradient of the scalar field $\hat{\nabla}\hat{\phi}$, the acceleration is given by

$$a = -\frac{c^2}{L}\frac{\mu^2}{\lambda M^2}\hat{\phi}\hat{\nabla}\hat{\phi}. \tag{5.41}$$

Inside a loop over time, the position and velocity of the test particle are updated via

$$v_{1/2} = v_{1/2} + a \ \mathrm{d}t, \tag{5.42a}$$

$$x = x + v_{1/2} \ \mathrm{d}t, \tag{5.42b}$$

after which the velocity is resynchronized with

$$v = v_{1/2} - \frac{1}{2} a \ \mathrm{d}t. \tag{5.43}$$

The use of a leapfrog algorithm involves the choice of a time step over which the simulation is run. If this time step is too large, the leapfrog algorithm no longer accurately captures the dynamics of the test particle; the particle could step over the domain wall and any insight into the particle's change in behaviour due to the presence of the domain wall will be lost. Conversely, if the time step is chosen to be very small, the computational time will be increased but the particle's trajectory will stay the same; below a certain size of time step, it will take longer to achieve the same result. We tested the leapfrog code with various time steps, and are confident that the chosen time step is small enough to accurately represent the motion of the particle.

5.4 Thin domain walls

For the thin domain wall case that we model, the width $d = 10^{-4}$ m of the domain wall is much smaller than the internal dimensions of the vacuum chamber. For this reason, we expect the motion of a test particle to be well-modelled by the analytic solution for an infinite and straight domain wall. We choose $\mu = 2 \times 10^{-13}$ GeV, $M = 100$ GeV and $\lambda = 10^{-10}$, corresponding to the left black dot in Figure 5.1. In the case that the initial position is $y_0 = 5 \times 10^{-3}$ m, the analytic solution in Section 5.1 suggests that particles with initial velocities of $\dot{y}_0 = 3 \times 10^{-3}$ ms^{-1} or below will be trapped in the potential

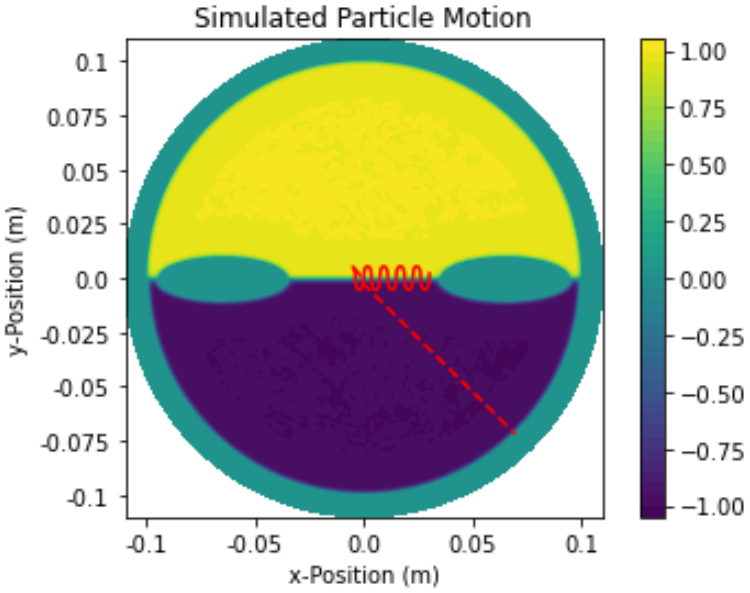

Figure 5.3: The motion of two test particles with initial position $(x_0, y_0) = (-0.005, 0.005)$ m and initial velocities $(\dot{x}_0, \dot{y}_0) = (10^{-3}, -10^{-3})$ ms^{-1} (solid curve) and $(\dot{x}_0, \dot{y}_0) = (10^{-2}, -10^{-2})$ ms^{-1} (dashed curve). We choose $\mu = 2 \times 10^{-13}$ GeV, $M = 100$ GeV and $\lambda = 10^{-10}$, corresponding to the left black dot in Figure 5.1. The colour bar indicates the value of the scalar field, with ϕ_0 normalized to 1. The simulation runs for $t = 35$ s. The particle with lower initial velocity gets trapped in the potential well of the domain wall and oscillates backwards and forwards across it; these oscillations are shown to scale in the figure. The particle with higher initial velocity has enough energy to escape the potential well and passes straight through the wall.

well of the domain wall, and particles with initial velocities higher than this will pass straight through the domain wall.

In Figure 5.3 we show the results of two numerical simulations for a thin domain wall, corresponding to two test particles with different initial velocities. The colourbar indicates the value of the scalar field, with ϕ_0 normalized to 1. The simulation runs for $t = 35$ s. We calculate the motion of each particle in the scalar field background using the leapfrog algorithm described in Section 5.3. We find that, as expected, a particle with initial velocity $(\dot{x}_0, \dot{y}_0) = (10^{-3}, -10^{-3})$ ms^{-1} is trapped by the domain wall: its path is shown by the solid red sinusoidal curve. The particle does not have enough energy to escape from the potential well of the symmetron field, so it oscillates backwards and forwards across the domain wall. The dashed red line in Figure 5.3 shows the path of a test particle with a higher initial velocity of $(\dot{x}_0, \dot{y}_0) = (10^{-2}, -10^{-2})$ ms^{-1}. This particle has enough energy to escape the potential well, and it therefore passes straight through the domain wall, in agreement with the analytic solution.

5.5 Thick domain walls

The second point in parameter space that we choose to explore in more detail corresponds to a thicker domain wall, and is indicated by the right black dot in Figure 5.1. In this case we have $\mu = 2 \times 10^{-14}$ GeV, $M = 10^4$ GeV and $\lambda = 10^{-10}$. The width of the domain wall is $d = 10^{-3}$ m, and the simulation runs for $t = 3000$ s. For a thicker domain wall, a test particle must be travelling at a much slower velocity than in the thin wall case in order for us to be able to observe the effects of the domain wall on the particle motion. We do not expect the effects of thick domain walls to be well-modelled by the analytic approximation for a thin and infinite domain wall in Section 5.1. We find that, for the values of initial velocity that we have simulated (down to $(\dot{x}_0, \dot{y}_0) = (10^{-5}, 10^{-5})$ ms^{-1}), the test particle always passes through the domain wall.

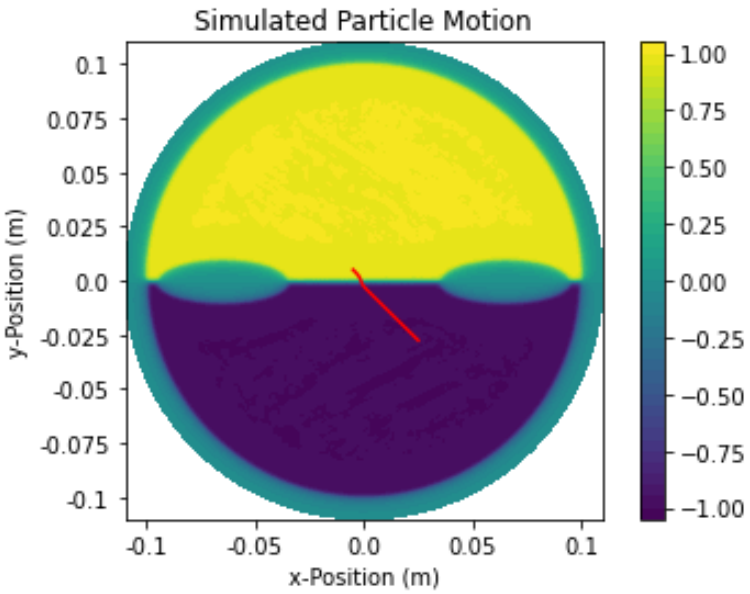

Figure 5.4: The motion of a test particle with initial position $(x_0, y_0) = (-0.005, 0.005)$ m and initial velocity $(\dot{x}_0, \dot{y}_0) = (10^{-5}, 10^{-5})$ ms^{-1}. We choose $\mu = 2 \times 10^{-14}$ GeV, $M = 10^4$ GeV and $\lambda = 10^{-10}$, corresponding to the right black dot in Figure 5.1. The colour bar indicates the value of the scalar field, with ϕ_0 normalized to 1. The simulation runs for $t = 3000$ s. The particle has enough energy to escape the potential well of the domain wall, and is able to travel through it. However, the trajectory of the particle is altered when it approaches the domain wall; it is deflected by the scalar fifth force.

Chapter 6

Coupling to Electromagnetism

We have thus far only considered the impact of the symmetron fifth force on an arbitrary test particle. By allowing the symmetron to couple to electromagnetism, we can contextualize our findings in terms of realizable experiments, both in the laboratory and in astronomical or cosmological settings. In this chapter, we study the dynamics of a photon coupled to a domain wall. By deriving a bound on the wavenumber k of the photon, we can find approximate numerical values for the reflection and transmission coefficients when the photon is incident on a domain wall. These values allow us to make some preliminary comments on the likelihood of observing the impact of a domain wall on the dynamics of a photon in experiment.

6.1 Equation of motion for a photon coupled to a symmetron

We can choose to introduce a coupling that respects the $\phi \to -\phi$ symmetry of the symmetron model. The equation of motion for a photon coupled to the symmetron field takes the form:

$$\nabla^\sigma \left(F_{\sigma\rho} \left(1 + \frac{4\phi^2}{M^2} \right) \right) = 0 \tag{6.1}$$

where the electromagnetic tensor $F_{\sigma\rho} = \partial_\sigma A_\rho - \partial_\rho A_\sigma$. The equation of motion comes from varying the Lagrangian of the photon with respect to the photon field A_μ [87]. We assume that the scalar field is a symmetron, which forms a static domain wall with a tanh profile solution given by

$$\phi = \phi_0 \tanh \frac{x}{d}. \tag{6.2}$$

We also assume the gauge condition

$$\partial_\alpha A^\alpha = 0. \tag{6.3}$$

Defining the function $f(x)$ as

$$f(x) = 1 + \frac{4\phi_0^2}{M^2} \tanh^2 \frac{x}{d}, \tag{6.4}$$

the equation of motion for the photon becomes

$$\nabla^\sigma \left(f(x)F_{\sigma\rho}\right) = 0. \tag{6.5}$$

Using the product rule, the equation of motion for the photon field A_μ is

$$\Box A_\mu + \frac{\nabla^\nu f}{f}\left(\nabla_\nu A_\mu - \nabla_\mu A_\nu\right) = 0. \tag{6.6}$$

As the function $f(x) \equiv f$ is only dependent on x, Equation 6.6 simplifies to

$$\Box A_\mu + \frac{f'}{f}\left(\nabla_x A_\mu - \nabla_\mu A_x\right) = 0. \tag{6.7}$$

The A_x equation is unchanged, and the A_y and A_z equations have the same form:

$$\Box A_x = 0 \tag{6.8a}$$

$$\Box A_y + \frac{f'}{f}\left(\nabla_x A_y - \nabla_y A_x\right) = 0 \tag{6.8b}$$

$$\Box A_z + \frac{f'}{f}\left(\nabla_x A_z - \nabla_z A_x\right) = 0. \tag{6.8c}$$

The equations of motion may also be written in terms of the electric and magnetic fields:

$$E_i = F_{0i} \tag{6.9a}$$

$$B_i = -\frac{1}{2}\epsilon_{ijk}F^{jk}. \tag{6.9b}$$

Following the logic laid out in ref. [87], we can use these equations to recover the modified Maxwell equations in the form

$$\underline{\nabla} \cdot \underline{\mathrm{B}} = 0 \tag{6.10a}$$

$$\underline{\nabla} \times \underline{\mathrm{E}} + \dot{\underline{\mathrm{B}}} = 0 \tag{6.10b}$$

$$\underline{\nabla} \cdot \left(f(x)\underline{\mathrm{E}}\right) = 0 \tag{6.10c}$$

$$\underline{\nabla} \times \left(f(x)\underline{\mathrm{B}}\right) = \partial_0 \left(f(x)\underline{\mathrm{E}}\right). \tag{6.10d}$$

Using Equation 6.9b, we find

$$\nabla \cdot B_i = \nabla_i \left(-\frac{1}{2}\right)\epsilon_{ijk}F^{jk} \tag{6.11}$$

$$= \frac{1}{2}\epsilon_{ijk}\nabla_i \left(\partial_j A_k - \partial_k A_j\right) \tag{6.12}$$

$$= 0 \tag{6.13}$$

$$\Rightarrow \underline{\nabla} \cdot \underline{\mathrm{B}} = 0 \tag{6.14}$$

where the third line follows from the antisymmetry of ϵ_{ijk}. Then taking the curl of the electric field $\underline{\mathrm{E}}$, we find

$$\begin{aligned}\underline{\nabla} \times \underline{\mathrm{E}} &= \epsilon_{ijk}\nabla_j E_k \\ &= \epsilon_{ijk}\nabla_j \left(\partial_0 A_k - \partial_k A_0\right) \\ &= \epsilon_{ijk}\partial_0 \nabla_j A_k, \end{aligned} \tag{6.15}$$

and $\dot{\underline{\mathrm{B}}}$ is given by

$$\begin{aligned}\dot{\underline{\mathrm{B}}} &= -\frac{1}{2}\epsilon_{ijk}\dot{F}_{jk} \\ &= -\frac{1}{2}\epsilon_{ijk}\left(\partial_j \dot{A}_k - \partial_k \dot{A}_j\right) \\ &= -\frac{1}{2}\epsilon_{ijk}\left(\epsilon_{ijk} - \epsilon_{ikj}\right) \\ &= -\frac{1}{2}\epsilon_{ijk}\left(\epsilon_{ijk} + \epsilon_{ijk}\right) \\ &= -\epsilon_{ijk}\partial_j \dot{A}_k. \end{aligned} \tag{6.16}$$

Therefore, we have

$$\underline{\nabla} \times \underline{\mathrm{E}} + \dot{\underline{\mathrm{B}}} = 0. \tag{6.17}$$

To find the third of the modified Maxwell equations, we use the equation of motion for the photon (Equation 6.44) and Equation 6.9a:

$$\begin{aligned}&\partial_\mu \left(f(x)F^{\mu 0}\right) = 0 \quad \& \quad \partial_\mu \left(f(x)F^{\mu i}\right) = 0 \\ &\Rightarrow -\partial_0 \left(f(x)F^{00}\right) + \partial_i \left(f(x)F^{i0}\right) = 0 \\ &\Rightarrow \underline{\nabla} \cdot \left(f(x)\underline{E}\right) = 0 \end{aligned} \tag{6.18}$$

where Equation 6.18 follows from the fact that $F^{00} = 0$. To find the final modified Maxwell equation, we start from

$$-\partial_0 \left(f(x)F^{0i}\right) + \partial_j \left(f(x)F^{ji}\right) = 0 \tag{6.19}$$

and take the curl of $f(x)\underline{\mathrm{B}}$ to find

$$\begin{aligned}
\underline{\nabla} \times (f(x)\underline{\mathrm{B}}) &= \epsilon_{ijk}\nabla_j \left(f(x)B_k\right) \\
&= \epsilon_{ijk}\nabla_j \left(f(x)\left(-\frac{1}{2}\right)\epsilon_{kpq}F^{pq}\right) \\
&= -\frac{1}{2}\nabla_j \left(f(x)\left(\partial_{ip}\partial_{jq} - \partial_{iq}\partial_{jp}\right)F^{pq}\right) \\
&= -\frac{1}{2}\nabla_j \left(f(x)\left(F^{ij} - F^{ji}\right)\right) \\
&= -\frac{1}{2}\nabla_j \left(2f(x)F^{ij}\right) \\
&= -\nabla_j \left(f(x)F^{ij}\right) \\
&= \nabla_j \left(f(x)F^{ij}\right). \qquad (6.20)
\end{aligned}$$

Therefore, we have

$$\begin{aligned}
-\partial_0 \left(f(x)\underline{\mathrm{E}}\right) + \underline{\nabla} \times (f(x)\underline{\mathrm{B}}) &= 0 \\
\Rightarrow \underline{\nabla} \times (f(x)\underline{\mathrm{B}}) &= \partial_0 \left(f(x)\underline{\mathrm{E}}\right). \qquad (6.21)
\end{aligned}$$

Assuming that $f \equiv f(x)$, the wave equations for the electric and magnetic fields associated to the modified Maxwell equations are then

$$\Box E_i + \frac{f'}{f}\nabla_x E_i = \delta_{ix}\left(\frac{f''}{f} - \frac{(f')^2}{f^2}\right)E_x \qquad (6.22a)$$

$$\Box B_i + \frac{f'}{f}\nabla_x B_i = (B_i - \delta_{ix}B_x)\left(\frac{f''}{f} - \frac{(f')^2}{f^2}\right) \qquad (6.22b)$$

In ref. [87], the second derivatives of f are neglected and the equation of motion for the electric field becomes

$$\Box E_i + \frac{f'}{f}\nabla_x E_i = 0. \qquad (6.23)$$

Upon making the assumption that the change in the dispersion relation is small, Equation 6.23 is solved to find the angular frequency ω:

$$\omega = k - \frac{if'k_x}{2fk} \qquad (6.24)$$

where k is the wavenumber, and the imaginary part is the dissipation term. Equation 6.23 shows that the domain wall, which has non-zero f', can change the amplitude of the electric wave as it passes through the wall. The second derivative terms in the full equation of motion for E_x can only be neglected when the following conditions are satisfied:

$$\frac{f'}{f} < k \qquad (6.25a)$$

$$f'' < f'k. \qquad (6.25b)$$

Assuming $f \approx 1$, these conditions require

$$\frac{8\phi_0^2}{dM^2} < k \tag{6.26a}$$

$$\text{and } 1 < kd. \tag{6.26b}$$

In the low frequency regime, the above conditions will be violated. We can investigate the behaviour of the photon's equation of motion in this regime, to see whether we can expect that electromagnetic waves will be reflected or transmitted through the domain wall. When the frequency is small, the equation of motion for E_x becomes

$$\Box E_x = -\left(\frac{f''}{f} - \frac{(f')^2}{f^2}\right) E_x. \tag{6.27}$$

Instead of neglecting the second derivatives of f as in ref. [87], we make the assumption that the domain wall is thin. We would like to find the behaviour of the term in brackets in Equation 6.27 in the limit $d \to 0$. Recalling the definition of the function $f(x)$,

$$f(x) = 1 + \frac{4\phi_0^2}{M^2} \tanh^2 \frac{x}{d}, \tag{6.28}$$

we have

$$f' = \frac{8\phi_0^2}{M^2 d} \operatorname{sech}^2 \frac{x}{d} \tanh \frac{x}{d} \tag{6.29a}$$

$$\text{and } f'' = \frac{8\phi_0^2}{M^2 d^2} \operatorname{sech}^4 \frac{x}{d} - \frac{16\phi_0^2}{M^2 d^2} \operatorname{sech}^2 \frac{x}{d} \tanh^2 \frac{x}{d}. \tag{6.29b}$$

Substituting the above expressions into the term in brackets in Equation 6.27 and integrating from $-\infty$ to ∞ results in

$$\int_{-\infty}^{\infty} \frac{f''}{f} - \frac{(f')^2}{f^2} \mathrm{d}x \simeq \int_{-\infty}^{\infty} f'' - (f')^2 \mathrm{d}x \tag{6.30}$$

$$= -\frac{256\phi_0^2}{15M^2 d} \tag{6.31}$$

where in the first line we approximate $f \approx 1$, since the dominant contribution comes from the f'' term. Equation 6.27 then becomes

$$\Box E_x = \frac{256\phi_0^2}{15M^2 d}\left(\frac{15M^2 d}{256\phi_0^2}\left[\frac{8\phi_0^2}{M^2 d^2} \operatorname{sech}^4 \frac{x}{d} - \frac{16\phi_0^2}{M^2 d^2} \operatorname{sech}^2 \frac{x}{d} \tanh^2 \frac{x}{d} - \left(\frac{8\phi_0^2}{M^2 d}\right)^2 \operatorname{sech}^4 \frac{x}{d} \tanh^2 \frac{x}{d}\right]\right) E_x$$

$$= \frac{256\phi_0^2}{15M^2 d}\left(\frac{15}{256d}\left[8 \operatorname{sech}^4 \frac{x}{d} - 16 \operatorname{sech}^2 \frac{x}{d} \tanh^2 \frac{x}{d} - \frac{64\phi_0^2}{M^2} \operatorname{sech}^4 \frac{x}{d} \tanh^2 \frac{x}{d}\right]\right) E_x \tag{6.32}$$

where the term in round brackets is a function that integrates to 1. We can now use the fact that for any integrable function $\eta(x)$ with

$$\int_{-\infty}^{\infty} \eta(x)\mathrm{d}x = 1, \tag{6.33}$$

the expression

$$\eta_\epsilon(x) = \frac{1}{\epsilon}\eta\left(\frac{x}{\epsilon}\right) \tag{6.34}$$

will approximate a delta function in the limit $\epsilon \to 0$. The expression in round brackets in Equation 6.32 is of the form in Equation 6.34, and we can therefore say that in the limit $d \to 0$, the term in round brackets can be approximated by $\delta(x)$. The equation of motion for the photon in the thin wall approximation is then simplified to

$$\Box E_x = \frac{256\phi_0^2}{15M^2 d}\delta\left(x\right)E_x. \tag{6.35}$$

6.2 Reflection & transmission coefficients for a domain wall coupled to a photon

As in Section 2.3, we can calculate the reflection and transmission coefficients of the domain wall coupled to a photon. The difference in this scenario is that instead of equations of motion for the domain wall and and a matter particle, we now have equations of motion for the domain wall and a photon. The equation of motion for the domain wall is the same as in Section 2.3:

$$\frac{\mathrm{d}^2\phi}{\mathrm{d}z}^2 = \lambda\phi\left(\phi^2 - \eta^2\right). \tag{6.36}$$

As shown in Section 6.1, the equation of motion for the photon coupled to the domain wall is given by

$$\Box E_x = \frac{256\phi_0^2}{15dM^2}\delta\left(x\right)E_x, \tag{6.37}$$

which can be written as

$$-\frac{\partial^2 E_x}{\partial t^2} + \frac{\partial^2 E_x}{\partial x^2} - \frac{256\phi_0^2}{15dM^2}\delta\left(x\right)E_x = 0 \tag{6.38}$$

for waves travelling in the x direction. The domain wall is located at $x = 0$. We would like to find two separate solutions to the above equation of motion, corresponding to either side of the domain wall where $x < 0$ and $x > 0$. The delta function $\delta(x)$ disappears everywhere apart from $x = 0$, so the equation of motion can be simplified to:

$$-\frac{\partial^2 E_x}{\partial t^2} + \frac{\partial^2 E_x}{\partial x^2} = 0. \tag{6.39}$$

Since this is very similar to a wave equation, we can make the following ansatz:

$$E_x(x,t) = \hat{E}_x(x)\mathrm{e}^{-ikt}. \tag{6.40}$$

Substituting this into the equation of motion, we find:

$$\frac{\partial^2 E_x}{\partial t^2} = -k^2 \hat{E}_x e^{-ikt} \tag{6.41a}$$

$$\frac{\partial^2 E_x}{\partial x^2} = \hat{E}_x'' e^{-ikt} \tag{6.41b}$$

where $'$ denotes a derivative with respect to x. Substituting Equations 6.41a and 6.41b into the equation of motion for the photon, we find

$$k^2 \hat{E}_x e^{-ikt} + \hat{E}_x'' e^{-ikt} = 0. \tag{6.42}$$

Writing the $\hat{E}_x$ in terms of E_x results in

$$\hat{E}_x = E_x e^{ikt} \tag{6.43a}$$

$$\hat{E}_x'' = E_x'' e^{ikt}, \tag{6.43b}$$

and the equation of motion for the photon therefore becomes

$$E_x'' + k^2 E_x = 0. \tag{6.44}$$

Equation 6.44 has the general solution

$$\begin{cases} E_L = Ae^{ikx} + Be^{-ikx} & x < 0 \\ E_R = Ce^{ikx} & x > 0 \end{cases} \tag{6.45}$$

where E_L is the solution on one side of the domain wall ($x < 0$) and E_R is the solution on the other ($x > 0$). Ae^{ikx} is the incident wave, Be^{-ikx} is the reflected wave and Ce^{ikx} is the transmitted wave. The reflection and transmission coefficients for the photon are dependent on the amplitudes A, B and C; we can calculate these reflection and transmission coefficients by imposing matching conditions across the domain wall at $x = 0$. Since the solution to the photon's equation of motion, E_x, must be continuous across the boundary, we have

$$E_L(0) = E_R(0) \tag{6.46}$$

which leads to the following relation between the amplitudes A, B and C:

$$A + B = C. \tag{6.47}$$

For the second matching condition, we note that the first derivative of the solution, E_x', is discontinuous across the domain wall by some amount that we will denote as Δ. To

calculate the size of this discontinuity, we can integrate the full equation of motion,

$$\begin{aligned} E_x'' + k^2 E_x - \frac{256\phi_0^2}{15dM^2}\delta(x)E_x &= 0 \\ \Rightarrow E_x'' &= -k^2 E_x + \frac{256\phi_0^2}{15dM^2}\delta(x)E_x, \end{aligned} \tag{6.48}$$

over a very small region either side of the wall, from $-\epsilon$ to ϵ. The size of the discontinuity is then given by

$$\Delta = E_R'(0) - E_L'(0) = \int_{-\epsilon}^{\epsilon} \mathrm{d}x E_x'' \tag{6.49}$$

$$\begin{aligned} &= \int_{-\epsilon}^{\epsilon} \mathrm{d}x \left(-k^2 E_x + \frac{256\phi_0^2}{15dM^2}\delta(x)E_x \right) \\ &= -k^2 \int_{-\epsilon}^{\epsilon} \mathrm{d}x E_x + \frac{256\phi_0^2}{15dM^2} \int_{-\epsilon}^{\epsilon} \mathrm{d}x \delta(x) E_x \\ &= -k^2 \int_{-\epsilon}^{\epsilon} \mathrm{d}x E_x + \frac{256\phi_0^2}{15dM^2} E_x(0) \end{aligned} \tag{6.50}$$

where in the last line we have used the sifting property of the delta function, $\int \mathrm{d}x f(x)\delta(x-a) = f(a)$. The first integral in Equation 6.50 can be evaluated by splitting it into two integrals between $-\epsilon$ and 0, and between 0 and ϵ:

$$\begin{aligned} \Delta &= -k^2 \left(\int_{-\epsilon}^{0} \mathrm{d}x E_L + k^2 \int_{0}^{\epsilon} \mathrm{d}x E_R \right) + \frac{256\phi_0^2}{15dM^2} E_x(0) \\ &= -k^2 \int_{-\epsilon}^{0} \mathrm{d}x E_L - k^2 \int_{0}^{\epsilon} \mathrm{d}x E_R + \frac{256\phi_0^2}{15dM^2} E_x(0). \end{aligned} \tag{6.51}$$

Substituting in the left and right solutions from Equation 6.45 results in

$$\begin{aligned} \Delta &= -k^2 \int_{-\epsilon}^{0} \mathrm{d}x \left(A e^{ikx} + B e^{-ikx} \right) - k^2 \int_{0}^{\epsilon} \mathrm{d}x C e^{ikx} + \frac{256\phi_0^2}{15dM^2} E_x(0) \\ &= -k^2 \left[\frac{A}{i\omega} e^{ikx} - \frac{B}{ik} e^{-i\omega x} \right]_{-\epsilon}^{0} - k^2 \left[\frac{C}{ik} e^{ikx} \right]_{0}^{\epsilon} + \frac{256\phi_0^2}{15dM^2} E_x(0) \\ &= -ik^3 (A - B - A e^{-ik\epsilon} + B e^{ik\epsilon} + C e^{ik\epsilon} - C) + \frac{256\phi_0^2}{15dM^2} E_x(0). \end{aligned} \tag{6.52}$$

Using the relation between the amplitudes, $A + B = C$, the equation for Δ simplifies to

$$\Delta = -ik^3(-2B - A e^{-ik\epsilon} + A e^{ik\epsilon} + 2B e^{ik\epsilon}) + \frac{256\phi_0^2}{15dM^2} E_x(0). \tag{6.53}$$

We can now impose that the region over which we have performed the integration, $-\epsilon$ to ϵ, is infinitely small. Taking the limit $\epsilon \to 0$ results in cancellation of the entire first term, and the equation for Δ becomes

$$\Delta = \frac{256\phi_0^2}{15dM^2} E_x(0). \tag{6.54}$$

Since the left and right solutions are equal at $x = 0$, $E_L(0) = E_R(0) = A + B$, we can write

$$E_x(0) = A + B, \tag{6.55}$$

so that

$$\Delta = \frac{256\phi_0^2}{15dM^2}(A + B). \tag{6.56}$$

We would like to eliminate Δ, in order to use the amplitudes A and B to calculate the reflection and transmission coefficients of the photon. Using the definition of Δ in Equation 6.49 and substituting in the left and right solutions to the equation of motion, we find

$$\begin{aligned}\Delta &= E'_R(0) - E'_L(0) \\ &= ikCe^{ikx}(0) - \left(ikAe^{ikx}(0) - ikBe^{-ikx}(0)\right) \\ &= ikC - ikA + ikB.\end{aligned} \tag{6.57}$$

Using $A + B = C$ to eliminate C results in a simple expression for Δ:

$$\Delta = 2ikB. \tag{6.58}$$

Equating this with the expression for Δ in Equation 6.56 leads to

$$\begin{aligned}&\frac{256\phi_0^2}{15dM^2}(A + B) = 2ikB \\ &\Rightarrow A = \frac{2ik - \frac{256\phi_0^2}{15dM^2}}{\frac{256\phi_0^2}{15dM^2}}B\end{aligned} \tag{6.59}$$

where in the second line we have written the amplitude of the incident wave (A) in terms of the amplitude of the reflected wave (B). The reflection coefficient of the photon incident on the domain wall is defined by $R = |B|^2/|A|^2$, so from Equation 6.59 we have

$$\begin{aligned}R = \frac{|B|^2}{|A|^2} &= \frac{|B|^2}{\left|\frac{2ik - \frac{256\phi_0^2}{15dM^2}}{\frac{256\phi_0^2}{15dM^2}}B\right|^2} \\ &= \frac{\frac{16384\phi_0^4}{d^2M^4}}{k^2 + \frac{16384\phi_0^4}{d^2M^4}}.\end{aligned} \tag{6.60}$$

Defining $\alpha^2 = 16384\phi_0^4/d^2M^4$, the reflection coefficient of the photon incident on the domain wall is given by

$$R = \frac{\alpha^2}{k^2 + \alpha^2}. \tag{6.61}$$

We may now also calculate the transmission coefficient T, which is defined by $T = 1 - R$:

$$\begin{aligned} T &= 1 - \frac{\alpha^2}{k^2 + \alpha^2} \\ \Rightarrow T &= \frac{k^2}{k^2 + \alpha^2}. \end{aligned} \tag{6.62}$$

In the following section, we put some approximate bounds on the wavenumber k; this will allow us to find some preliminary numerical estimates for the reflection and transmission coefficients of a photon coupled to a domain wall.

6.3 Bounds on the wavenumber k

6.3.1 First estimate

Putting a bound on the wavenumber k will allow us to gain some insight into what kinds of frequencies would be required for an experiment involving a domain wall coupled to a photon to produce observable results. To do this, we use the bound in Equation 6.26a:

$$\frac{8\phi_0^2}{dM^2} < k \tag{6.63}$$

and insert the numerical values used in our test particle simulation in Chapter 5. We choose the thin domain wall simulation, for which the values of d and M are

$$d = 10^{-3} \text{ m} \tag{6.64a}$$

$$M = 100 \text{ GeV}. \tag{6.64b}$$

To keep the units consistent, we put the domain wall width d in GeV, and substitute both values into the bound on k, resulting in

$$\begin{aligned} &\frac{8\phi_0^2}{\frac{1}{1.9733\times10^{-13}} \text{ GeV}^{-1} \times (100 \text{ GeV})^2} < k \\ &\Rightarrow 1.57864 \times 10^{-16}\phi_0^2 \text{ GeV}^{-1} < k. \end{aligned} \tag{6.65}$$

The quantity ϕ_0 is given by

$$\phi_0^2 = \frac{\mu^2}{\lambda}\left(1 - \frac{\rho_0}{\rho_*}\right). \tag{6.66}$$

We can assume that $\rho_* \gg \rho_0$, such that the second term inside the parentheses is negligible and

$$\phi_0^2 = \frac{\mu^2}{\lambda}. \tag{6.67}$$

For a domain wall of width $d = 10^{-4}$m, the corresponding value of μ in our test particle simulation is:

$$\mu = 1.97 \times 10^{-13} \text{ GeV} \tag{6.68}$$

and we choose $\lambda = 10^{-10}$. Substituting these values into the above equation for ϕ_0^2, we find

$$\phi_0^2 = 3.8809 \times 10^{-16}\ \text{GeV}^2, \tag{6.69}$$

and the bound on the wavenumber k is then

$$6.13 \times 10^{-32}\ \text{GeV} < k \tag{6.70}$$

to 3 significant figures. The wavenumber k is inversely proportional to the frequency, so that a very small k corresponds to very high frequencies, and short wavelengths. To observe the effects of domain walls in astronomical or cosmological experiments, the wavelength should be on the scale of tens of metres to hundreds of metres. In a tabletop experiment such as the test particle simulation in Chapter 5, the wavelength should instead be approximately between 10 cm and 10 m. The bound in Equation 6.70 corresponds to vastly larger wavelengths than either of these experimental scenarios, and thus does not represent a set of parameters which would lead to observable effects. We would therefore like to shift the bound on k upwards. This can be done in various ways, including making the width of the domain wall smaller, or using a smaller value of the coupling constant λ. In the following section, we demonstrate how the bound on k can be shifted to align with more realistic experimental parameters, by using a smaller value of λ.

6.3.2 Shifting the bound on k

There is motivated parameter space for values of the coupling constant λ smaller than 10^{-10}, as illustrated in Figure 5.2. Figure 5.2 shows the parameter space for $\lambda = 10^{-30}$. We choose a point in the bottom left part of the plot which is not excluded by existing constraints from atom interferometry, with the following values of d and M:

$$d = 10^{-5}\ \text{m} \tag{6.71a}$$

$$M = 10\ \text{GeV}. \tag{6.71b}$$

Putting d in units of GeV and substituting into the bound on k, we find

$$\begin{aligned} &\frac{8\phi_0^2}{\frac{1}{1.9733\times10^{-11}}\ \text{GeV}^{-1} \times (10\ \text{GeV})^2} < k \\ &\Rightarrow 1.57864 \times 10^{-12}\phi_0^2\ \text{GeV}^{-1} < k. \end{aligned} \tag{6.72}$$

These values of d and M correspond to $\mu = 1.97 \times 10^{-11}$ GeV in our test particle simulation. ϕ_0^2 is then given by

$$\begin{aligned} \phi_0^2 &= \frac{\mu^2}{\lambda} \\ &= 388090000\ \text{GeV}^2 \end{aligned} \tag{6.73}$$

and the bound on k is

$$6.13 \times 10^{-4} \text{ GeV} < k \tag{6.74}$$

to three significant figures. These larger values of the wavenumber are associated with wavelengths on the order of 10^4 m, which is much closer than our first estimate to the parameter space in which we expect experimental observations to be possible. If a network of domain walls exists in the universe, it could have a detectable impact on radio observables.

6.3.3 Numerical values for the reflection and transmission coefficients

Using the bound on the wavenumber k that we calculated in Section 6.3.2, we can find some approximate numerical values for the reflection and transmission coefficients associated with the photon incident on the domain wall. As in Section 6.3.2, we choose a point in the parameter space plot for $\lambda = 10^{-30}$ corresponding to the following values of d and M:

$$d = 10^{-5}\text{m} = \frac{1}{1.9733 \times 10^{-13}} \text{ GeV}^{-1} \tag{6.75a}$$

$$M = 10 \text{ GeV}. \tag{6.75b}$$

These values of d and M correspond to $\mu = 1.97 \times 10^{-11}$ GeV in our test particle simulation. This choice of μ is different from that in Chapter 5, since we are now using $\lambda = 10^{-30}$ rather than $\lambda = 10^{-10}$. The value of ϕ_0^2 is given by

$$\phi_0^2 = \frac{\mu^2}{\lambda} = 388090000 \text{ GeV}^2. \tag{6.76}$$

We can now calculate the constant α that we defined previously:

$$\alpha^2 = \frac{16384\phi_0^4}{d^2M^4} \Rightarrow \alpha = \frac{128\phi_0^2}{dM^2} = 9.80 \times 10^{-5} \text{ GeV} \tag{6.77}$$

to three significant figures. Substituting this value of α into the expression for the reflection coefficient $R = \alpha^2/(k^2 + \alpha^2)$ leads to

$$R = 0.025 \tag{6.78}$$

to two significant figures. Using the fact that the transmission coefficient T is defined by $T = 1 - R$, we can write T as

$$T = 0.975 \tag{6.79}$$

to three significant figures. The physical interpretation of these reflection and transmission coefficients is that in our idealized experiment, 25 in every 1000 photons that are incident on the domain wall will be reflected back. It is important to note that our model is subject to simplifications, and the calculated values of reflection and transmission coefficients must therefore be viewed as preliminary approximations. However, we can conclude that such a high proportion of reflected photons is promising for the possible detection of the effect of the symmetron fifth force when domain walls couple to electro-

magnetism, especially in astronomical or cosmological contexts where the frequency of electromagnetic radiation is very high. In the context of tabletop experiments, photon reflection could be observed using a highly sensitive camera that can detect very low light levels. These types of instruments are used in light-shining-through-walls experiments to search for axions (see ref. [88] for an example).

Chapter 7

Conclusions & Future Work

In this work we have proposed an experiment to detect the effects that topological defects called 'domain walls' which mediate the fifth force can have on matter particles. In Chapter 1 we introduce the concept of new light scalar fields that couple to gravity, and how screening models such as the symmetron have the potential to constrain some previously unconstrained parts of the dark sector. We describe how domain walls form through spontaneous symmetry breaking, and discuss previous numerical studies of domain wall formation. We summarize the existing constraints on the symmetron model from cosmological, laboratory and astrophysical tests, and consider some ways in which ultracold atoms can be used in tabletop experiments to observe the effects of domain walls on matter.

In Chapter 2, we specialize to the spherically symmetric symmetron field, and show how its equation of motion can be solved to yield a domain wall solution. Using this solution along with the wave equation for a particle approaching the domain wall, we derive expressions for the reflection and transmission coefficients arising from the interaction between the particle and the wall. We use the simplified model of plane waves reflecting off an infinite straight domain wall. Although this is not a realistic scenario, the fact that the impact of the domain wall is evident in the reflection and transmission coefficients leads us to believe that this is an experimentally interesting signature that warrants further investigation. Chapter 3 introduces the concept of our experiment to trap domain walls using a topologically-tailored vacuum chamber. We describe how domain walls can form via the Kibble–Zurek mechanism, and propose some idealized experimental scenarios in which a domain wall is pinned to matter overdensities in the chamber in the form of spikes that protrude from the chamber walls.

Chapter 4 details how the finite element software package SELCIE can be used to find vacuum solutions for the chameleon field around a user-defined source, and how we have modified the code to solve for the symmetron field. We describe the results of some initial simulations involving two identical sources inside the chamber, and show how

spatially-varying initial conditions of the field can result in a static domain wall solution. In Chapter 5, we present our main results: the numerical simulation of the motion of a test particle approaching a domain wall formed through the symmetron mechanism. We show that for different widths of the domain wall, the test particle is affected by the fifth force gradient mediated by the wall and its motion is altered. In the case of a thin wall, a particle with low initial velocity can be trapped in the potential well of the domain wall and oscillate backwards and forwards across it. If observed in experiment, this modification of a particle's motion in the presence of a domain wall would constitute a clear signature of the fifth force associated with the symmetron field.

Chapter 6 explores the possibility that the symmetron field can couple to electromagnetism. We choose to introduce a coupling that respects the $\phi \to -\phi$ symmetry of the symmetron model, and use the new equation of motion for the symmetron to derive an equation of motion for a photon coupled to the symmetron. By deriving some approximate bounds on the wavenumber k, we are able to calculate numerical values for the reflection and transmission coefficients associated with a photon approaching a domain wall. In our idealized experimental scenario, we show that 25 in every 1,000 photons that are incident on the domain wall will be reflected back.

There are many ways in which the work presented here can be built upon. One obvious goal is that the vacuum chamber experiment described in Chapter 3 and simulated in Chapter 5 can be realized experimentally. Such a vacuum chamber could be manufactured using state-of-the-art 3D printing technology [76]. In order for the vacuum chamber to be built to the required specifications, we must first model the vacuum chamber more accurately; in this work we have assumed that the vacuum chamber is spherical, but in reality it is more likely to be cylindrical. The particulars of the particle experiment performed inside the chamber will also need to be decided upon; these include the type of ultracold atom used, and the method of detecting the effect of the fifth force on these ultracold atoms (for example, atom interferometry).

In our initial simulations of a test particle approaching a domain wall, we have chosen the simple geometry of two ellipses as matter densities which pin the domain wall in place. Although we have shown that this choice of modified vacuum chamber interior results in a domain wall solution, we have not yet explored how a different distribution of spikes inside the chamber could affect the domain wall dynamics. Using a genetic algorithm or a machine learning algorithm, we could optimize the matter distribution such that the domain wall is as long-lived as possible, giving us more time to perform particle experiments to observe the effect that the fifth force gradient of the domain wall has on matter. It could also be possible to encourage the formation of a network of domain walls inside the chamber; such an experimental scenario is advantageous because the probability of observing a deflection or reflection of a particle off a domain wall increases as the number of potential interactions between matter and domain walls

increases.

Thus far, we have studied the interaction of a test particle with the static domain wall solution. For the formation and dynamics of domain walls in our vacuum chamber experiment to be investigated thoroughly, a time-dependent numerical simulation of the symmetron field is essential. If we can model how domain walls are formed and how they evolve over time, we can comment on their stability; knowledge of the stability of the domain walls will inform the optimization procedure for the matter distribution inside the vacuum chamber. The combination of a time-dependent model of the domain wall dynamics with an interior topology optimized for trapping and stabilizing domain walls will give us the best chance of detecting the effects of the symmetron fifth force in experiment.

Bibliography

[1] J. Khoury and A. Weltman. Chameleon fields: Awaiting surprises for tests of gravity in space. *Physical review letters*, 93(17):171104, 2004.

[2] S. S. Gubser and J. Khoury. Scalar self-interactions loosen constraints from fifth force searches. *Physical Review D*, 70(10):104001, 2004.

[3] D. J. Kapner et al. Tests of the gravitational inverse-square law below the dark-energy length scale. *Physical review letters*, 98(2):021101, 2007.

[4] S. Schlamminger et al. Test of the equivalence principle using a rotating torsion balance. *Physical Review Letters*, 100(4):041101, 2008.

[5] J. Khoury and A. Weltman. Chameleon cosmology. *Physical Review D*, 69(4):044026, 2004.

[6] K. Hinterbichler and J. Khoury. Screening long-range forces through local symmetry restoration. *Physical review letters*, 104(23):231301, 2010.

[7] M. Pospelov et al. Detecting domain walls of axionlike models using terrestrial experiments. *Physical review letters*, 110(2):021803, 2013.

[8] A. Derevianko and M. Pospelov. Hunting for topological dark matter with atomic clocks. *Nature Physics*, 10(12):933–936, 2014.

[9] Y. Stadnik and V. Flambaum. Searching for topological defect dark matter via nongravitational signatures. *Physical review letters*, 113(15):151301, 2014.

[10] Y. V. Stadnik and V. V. Flambaum. New atomic probes for dark matter detection: Axions, axion-like particles and topological defects. *Modern Physics Letters A*, 29(37):1440007, 2014.

[11] Y. V. Stadnik. New bounds on macroscopic scalar-field topological defects from nontransient signatures due to environmental dependence and spatial variations of the fundamental constants. *Physical Review D*, 102(11):115016, 2020.

[12] K. Hinterbichler et al. Symmetron cosmology. *Physical Review D*, 84(10):103521, 2011.

[13] A. Vilenkin and E. P. S. Shellard. *Cosmic strings and other topological defects*. Cambridge University Press, 1994.

[14] T. H. R. Skyrme. A non-linear field theory. *Proceedings of the Royal Society of London. Series A. Mathematical and Physical Sciences*, 260(1300):127–138, 1961.

[15] D. Finkelstein. Internal structure of spinning particles. *Physical Review*, 100(3):924, 1955.

[16] D. Finkelstein and J. Rubinstein. Connection between spin, statistics, and kinks. *Journal of Mathematical Physics*, 9(11):1762–1779, 1968.

[17] Y. Tanikawa. Proceedings of the International Conference on elementary particles, in commemoration of the 30 th Anniversary of Meson theory(Kyoto, 24 th-30 th Sept. 1965), 1966.

[18] Y. B. Zeldovich, I. Y. Kobzarev, and L. B. Okun. Cosmological Consequences of the Spontaneous Breakdown of Discrete Symmetry. *Zh. Eksp. Teor. Fiz.*, 67:3–11, 1974.

[19] S. Weinberg. Gauge and global symmetries at high temperature. *Phys. Rev. D*, 9:3357–3378, 12 June 1974.

[20] A. E. Everett. Observational consequences of a "domain" structure of the universe. *Phys. Rev. D*, 10:3161–3166, 10 Nov. 1974.

[21] T. W. Kibble. Topology of cosmic domains and strings. *Journal of Physics A: Mathematical and General*, 9(8):1387, 1976.

[22] W. H. Press, B. S. Ryden, and D. N. Spergel. Dynamical evolution of domain walls in an expanding universe. *Astrophysical Journal, Part 1 (ISSN 0004-637X), vol. 347, Dec. 15, 1989, p. 590-604. Research supported by NASA and Alfred P. Sloan Foundation.*, 347:590–604, 1989.

[23] L. Kawano. Evolution of Domain Walls in the Early Universe. *Phys. Rev. D*, 41:1013, 1990.

[24] A.-C. Davis et al. Structure formation in the symmetron model. *The Astrophysical Journal*, 748(1):61, 2012.

[25] B. Li et al. ECOSMOG: an efficient code for simulating modified gravity. *Journal of Cosmology and Astroparticle Physics*, 2012(01):051, 2012.

[26] M. Baldi. Dark energy simulations. *Physics of the Dark Universe*, 1(1-2):162–193, 2012.

[27] F. Schmidt. Self-consistent cosmological simulations of DGP braneworld gravity. *Physical Review D—Particles, Fields, Gravitation, and Cosmology*, 80(4):043001, 2009.

[28] C. Llinares and L. Pogosian. Domain walls coupled to matter: the symmetron example. *Physical Review D*, 90(12):124041, 2014.

[29] J. A. Pearson. Simulating the symmetron: Domain walls and symmetry-restoring impurities. *Physical Review D*, 90(12):125011, 2014.

[30] A. P. Naik and C. Burrage. Dark sector domain walls could explain the observed planes of satellites. *Journal of Cosmology and Astroparticle Physics*, 2022(08):020, 2022.

[31] B. Nosrati and N. Khosravi. Cosmic voids are emptier in the presence of symmetron's domain walls. *Physical Review D*, 108(8):083511, 2023.

[32] K. Nakayama, F. Takahashi, and N. Yokozaki. Gravitational waves from domain walls and their implications. *Physics Letters B*, 770:500–506, 2017.

[33] K. Saikawa. A review of gravitational waves from cosmic domain walls. *Universe*, 3(2):40, 2017.

[34] R. Z. Ferreira et al. Gravitational waves from domain walls in Pulsar Timing Array datasets. *Journal of Cosmology and Astroparticle Physics*, 2023(02):001, 2023.

[35] E. Babichev et al. NANOGrav spectral index $\gamma = 3$ from melting domain walls. *Physical Review D*, 108(12):123529, 2023.

[36] Ø. Christiansen, F. Hassani, and D. F. Mota. asimulation: Domain formation and impact on observables in resolved cosmological simulations of the (a) symmetron. *arXiv preprint arXiv:2401.02410*, 2024.

[37] Ø. Christiansen et al. Gravitational waves from dark domain walls. *arXiv preprint arXiv:2401.02409*, 2024.

[38] P. Brax et al. Testing screened modified gravity. *Universe*, 8(1):11, 2021.

[39] B. Bertotti, L. Iess, and P. Tortora. A test of general relativity using radio links with the Cassini spacecraft. *Nature*, 425(6956):374–376, 2003.

[40] S. Saito et al. Understanding higher-order nonlocal halo bias at large scales by combining the power spectrum with the bispectrum. *Physical Review D*, 90(12):123522, 2014.

[41] J. G. Williams, S. G. Turyshev, and D. H. Boggs. Progress in lunar laser ranging tests of relativistic gravity. *Physical Review Letters*, 93(26):261101, 2004.

[42] S. K. Lamoreaux. Demonstration of the Casimir force in the 0.6 to 6 μ m range. *Physical Review Letters*, 78(1):5, 1997.

[43] A. Upadhye. Symmetron dark energy in laboratory experiments. *Physical review letters*, 110(3):031301, 2013.

[44] R. Decca et al. Tests of new physics from precise measurements of the Casimir pressure between two gold-coated plates. *arXiv preprint hep-ph/0703290*, 2007.

[45] E. Adelberger and E.-W. GROUP. Sub-millimeter tests of the gravitational inverse square law. In: *CPT and Lorentz Symmetry*. World Scientific, 2002, 9–15.

[46] P. Brax et al. f (R) gravity and chameleon theories. *Physical Review D*, 78(10):104021, 2008.

[47] A. Upadhye. Dark energy fifth forces in torsion pendulum experiments. *Physical Review D*, 86(10):102003, 2012.

[48] P. Brax and G. Pignol. Strongly coupled chameleons and the neutronic quantum bouncer. *Physical Review Letters*, 107(11):111301, 2011.

[49] P. Brax, G. Pignol, and D. Roulier. Probing strongly coupled chameleons with slow neutrons. *Physical Review D*, 88(8):083004, 2013.

[50] B. Clément et al. Manipulation of gravitational quantum states of a bouncing neutron with the GRANIT spectrometer. *arXiv preprint arXiv:2205.11130*, 2022.

[51] P. Brax and M. Pitschmann. Exact solutions to nonlinear symmetron theory: one-and two-mirror systems. *Physical Review D*, 97(6):064015, 2018.

[52] M. Kasevich and S. Chu. Atomic interferometry using stimulated Raman transitions. *Physical review letters*, 67(2):181, 1991.

[53] A. D. Cronin, J. Schmiedmayer, and D. E. Pritchard. Optics and interferometry with atoms and molecules. *Reviews of Modern Physics*, 81(3):1051, 2009.

[54] P. Hamilton et al. Atom-interferometry constraints on dark energy. *Science*, 349(6250):849–851, 2015.

[55] B. Elder et al. Chameleon dark energy and atom interferometry. *Physical Review D*, 94(4):044051, 2016.

[56] C. Burrage, E. J. Copeland, and E. Hinds. Probing dark energy with atom interferometry. *Journal of Cosmology and Astroparticle Physics*, 2015(03):042, 2015.

[57] C. Burrage and E. J. Copeland. Using atom interferometry to detect dark energy. *Contemporary Physics*, 57(2):164–176, 2016.

[58] M. Jaffe et al. Testing sub-gravitational forces on atoms from a miniature in-vacuum source mass. *Nature Physics*, 13(10):938–942, 2017.

[59] D. O. Sabulsky et al. Experiment to detect dark energy forces using atom interferometry. *Physical Review Letters*, 123(6):061102, 2019.

[60] C. Burrage et al. Constraining symmetron fields with atom interferometry. *Journal of Cosmology and Astroparticle Physics*, 2016(12):041, 2016.

[61] P. Brax et al. Collider constraints on interactions of dark energy with the Standard Model. *Journal of High Energy Physics*, 2009(09):128, 2009.

[62] C. Burrage et al. Fifth-force screening around extremely compact sources. *Journal of Cosmology and Astroparticle Physics*, 2021(08):052, 2021.

[63] P. Brax, A.-C. Davis, and B. Elder. (g-2) μ and screened modified gravity. *Physical Review D*, 106(4):044040, 2022.

[64] C. Burrage, E. J. Copeland, and P. Millington. Radial acceleration relation from symmetron fifth forces. *Physical Review D*, 95(6):064050, 2017.

[65] F. Lelli et al. One law to rule them all: the radial acceleration relation of galaxies. *The Astrophysical Journal*, 836(2):152, 2017.

[66] L. Hui, A. Nicolis, and C. W. Stubbs. Equivalence principle implications of modified gravity models. *Physical Review D—Particles, Fields, Gravitation, and Cosmology*, 80(10):104002, 2009.

[67] B. Jain and J. VanderPlas. Tests of modified gravity with dwarf galaxies. *Journal of Cosmology and Astroparticle Physics*, 2011(10):032, 2011.

[68] H. Desmond et al. The fifth force in the local cosmic web. *Monthly Notices of the Royal Astronomical Society: Letters*, 483(1):L64–L68, 2019.

[69] H. Desmond et al. Fifth force constraints from the separation of galaxy mass components. *Physical Review D*, 98(6):064015, 2018.

[70] H. Desmond et al. Fifth force constraints from galaxy warps. *Physical Review D*, 98(8):083010, 2018.

[71] H. Desmond and P. G. Ferreira. Galaxy morphology rules out astrophysically relevant Hu-Sawicki f (R) gravity. *Physical Review D*, 102(10):104060, 2020.

[72] D.-C. Dai, D. Minic, and D. Stojkovic. Interaction of cosmological domain walls with large classical objects, like planets and satellites, and the flyby anomaly. *Journal of High Energy Physics*, 2022(3):1–17, 2022.

[73] C. Llinares and P. Brax. Detecting coupled domain walls in laboratory experiments. *Physical Review Letters*, 122(9):091102, 2019.

[74] H. Lemmel et al. Neutron interferometry constrains dark energy chameleon fields. *Physics Letters B*, 743:310–314, 2015.

[75] T. Jenke et al. Realization of a gravity-resonance-spectroscopy technique. *Nature Physics*, 7(6):468–472, 2011.

[76] N. Cooper et al. Additively manufactured ultra-high vacuum chamber for portable quantum technologies. *Additive manufacturing*, 40:101898, 2021.

[77] C. Briddon et al. SELCIE: a tool for investigating the chameleon field of arbitrary sources. *Journal of Cosmology and Astroparticle Physics*, 2021(12):043, 2021.

[78] C. Burrage, B. Elder, and P. Millington. Particle level screening of scalar forces in 1+ 1 dimensions. *Physical Review D*, 99(2):024045, 2019.

[79] W. H. Zurek. Cosmological experiments in superfluid helium? *Nature*, 317(6037):505–508, 1985.

[80] V. L. Ginzburg. Certain theoretical aspects of radiation due to superluminal motion in a medium. *Soviet Physics Uspekhi*, 2(6):874, 1960.

[81] M. Alnæs et al. The FEniCS project version 1.5. *Archive of numerical software*, 3(100), 2015.

[82] C. Geuzaine and J.-F. Remacle. Gmsh: A 3-D finite element mesh generator with built-in pre-and post-processing facilities. *International journal for numerical methods in engineering*, 79(11):1309–1331, 2009.

[83] T. Damour and J. F. Donoghue. Equivalence principle violations and couplings of a light dilaton. *Physical Review D—Particles, Fields, Gravitation, and Cosmology*, 82(8):084033, 2010.

[84] K. Clements et al. Detecting dark domain walls through their impact on particle trajectories in tailored ultrahigh vacuum environments. *Phys. Rev. D*, 109:123023, 12 June 2024.

[85] T. Jenke et al. Gravity resonance spectroscopy and dark energy symmetron fields. *The European Physical Journal Special Topics*, 230(4):1131–1136, 2021.

[86] A. Upadhye, W. Hu, and J. Khoury. Quantum stability of chameleon field theories. *Physical Review Letters*, 109(4):041301, 2012.

[87] V. V. Khoze and D. L. Milne. Optical effects of domain walls. *Physics Letters B*, 829:137044, 2022.

[88] R. Bähre et al. Any light particle search II—technical design report. *Journal of Instrumentation*, 8(09):T09001, 2013.